

On the maximum magnetic field amplification by the magnetorotational instability in core-collapse supernovae

T. Rembiasz^{1,2*}, J. Guilet^{1,3}, M. Obergaulinger², P. Cerdá-Durán², M.A. Aloy², E. Müller¹

¹ Max-Planck-Institut für Astrophysik, Karl-Schwarzschild-Str. 1, 85748 Garching, Germany

² Departamento de Astronomía y Astrofísica, Universidad de Valencia, C/Dr. Moliner 50, 46100 Burjassot, Spain

³ Max Planck/Princeton Center for Plasma Physics, Karl-Schwarzschild-Str. 1, 85748 Garching, Germany

Accepted 2016 May 16. Received 2016 April 28; in original form 2016 February 29

ABSTRACT

Whether the magnetorotational instability (MRI) can amplify initially weak magnetic fields to dynamically relevant strengths in core collapse supernovae is still a matter of active scientific debate. Recent numerical studies have shown that the first phase of MRI growth dominated by channel flows is terminated by parasitic instabilities of the Kelvin-Helmholtz type that disrupt MRI channel flows and quench further magnetic field growth. However, it remains to be properly assessed by what factor the initial magnetic field can be amplified and how it depends on the initial field strength and the amplitude of the perturbations. Different termination criteria leading to different estimates of the amplification factor were proposed within the parasitic model. To determine the amplification factor and test which criterion is a better predictor of the MRI termination, we perform three-dimensional shearing-disc and shearing-box simulations of a region close to the surface of a differentially rotating proto-neutron star in non-ideal MHD with two different numerical codes. We find that independently of the initial magnetic field strength, the MRI channel modes can amplify the magnetic field by, at most, a factor of 100. Under the conditions found in proto-neutron stars a more realistic value for the magnetic field amplification is of the order of 10. This severely limits the role of the MRI channel modes as an agent amplifying the magnetic field in proto-neutron stars starting from small seed fields. A further amplification should therefore rely on other physical processes, such as for example an MRI-driven turbulent dynamo.

Key words: accretion, accretion discs - MHD - instabilities - stars: magnetic field - supernovae: general

1 INTRODUCTION

Originally discovered by Velikhov (1959) and Chandrasekhar (1960), the magnetorotational instability (MRI) was suggested by Balbus & Hawley (1991) to be the physical mechanism driving the redistribution of angular momentum required for the accretion process in Keplerian discs orbiting compact objects (see, e.g. Balbus & Hawley 1998, for a review).

Keplerian discs have a positive radial gradient in angular momentum, and therefore are linearly (Rayleigh-)stable. Purely hydrodynamic perturbations are unlikely to grow to amplitudes at which the associated stresses can account for efficient angular-momentum transport. In the presence of a weak magnetic field, however, a negative radial gradient in the angular velocity of the disc is magnetorotationally unstable, and seed perturbations can grow exponentially on time scales close to the rotational period. During this phase, *channel modes* develop. Channel modes are pairs of coher-

ent radial up- and down-flows stacked vertically and threaded by layers of magnetic field of alternating radial and azimuthal polarity. In these modes, the magnetic tension (Maxwell stress tensor) transports angular momentum from the inner parts of the disc outwards.

The criterion for the MRI onset can be formulated in a rather simple manner, even if the thermal stratification (gradients of entropy or molecular weight) and non-ideal effects (viscosity, resistivity) are included (Balbus 1995; Menou et al. 2004). This allows for its application beyond Keplerian discs, in particular to proto-neutron stars (PNS) resulting from the core-collapse of rotating massive stars. Simplified simulations by Akiyama et al. (2003) showed that such PNSs possess regions in which the MRI can grow on shorter time scales than the time between the bounce and the successful explosion. This finding, later confirmed in multi-dimensional models (e.g. Obergaulinger et al. 2006b; Cerdá-Durán et al. 2008; Sawai et al. 2013; Sawai & Yamada 2015; Mösta et al. 2015), presents the possibility of generating strong magnetic fields that can tap the rotational energy of the core, power MHD turbu-

* E-mail: tomasz.rembiasz@uv.es

lence (Masada et al. 2015), and become a potentially important ingredient in rapidly-rotating core collapse supernovae (CCSNe).

How much these systems are affected by the MRI crucially depends on both its growth rate and on the final amplitude to which the seed perturbations grow. We can give an upper limit by assuming that the MRI ceases to grow once the magnetic field comes close to equipartition with the energy of the differential rotation. In a CCSN, this would correspond to dynamically important field strengths of $\sim 10^{15}$ G (see e.g. Meier et al. 1976; Obergaulinger et al. 2006b; Cerdá-Durán et al. 2008).

However, this estimate is an upper bound, since it neglects any effect quenching the MRI before it taps all the available differential rotation energy. The physics of the saturation of the MRI growth remains an active field of research with many studies devoted to finding the value of the α parameter (Shakura & Sunyaev 1973) for the stress tensor. We refer, among others, to the works of Sano et al. (2004); Sano & Inutsuka (2001); Brandenburg (2005); Fromang & Papaloizou (2007); Gardiner & Stone (2005); Knobloch & Julien (2005).

The model of parasitic instabilities by Goodman & Xu (1994, GX94 hereafter), further studied and developed by Latter et al. (2009), Pessah & Goodman (2009, PG09 hereafter) and Pessah (2010) provides a clear physical picture of the termination mechanism. The MRI channel modes are characterised by a shear layer and a current sheet in the vertical profiles of velocity and magnetic field, respectively. Hence, the (laminar) channel flows can be unstable against *secondary* (or *parasitic*) instabilities of Kelvin-Helmholtz (KH) or tearing-mode (TM) type.¹ Initially, the role of the parasites is negligible, as they grow much more slowly than the MRI. However, since the growth rate of the secondary instabilities is proportional to the channel mode amplitude (which grows exponentially with time), it is clear that at some stage the parasites will grow faster than the MRI channels (whose growth rate is constant). Roughly at this point, the parasitic instabilities should disrupt the channel modes and terminate the MRI growth, marking the transition to the turbulent saturation phase (PG09).

Pessah (2010) analytically studied the MRI termination in resistive-viscous MHD by solving simplified model equations for the evolution of the parasitic instabilities. He identified different parameter-space regimes where, depending on hydrodynamic and magnetic Reynolds numbers, either the KH instability or the TM is the dominant (i.e. faster developing) secondary instability. In the regime relevant for CCSNe, the MRI should be terminated by the KH instability.

Some of the predictions of the parasitic model have been confirmed by Rembiasz et al. (2016a), who performed semi-global MRI simulations of a PNS following Obergaulinger et al. (2009). They found, that given the CCSNe conditions, the MRI growth is indeed terminated by secondary parasitic KH instabilities. Moreover, the properties of these secondary instabilities were in a good agreement with the parasitic model. As expected, the parasitic instabilities developed along the velocity channels, displaying a very good agreement of the orientation under which the parasites develop, whereas the wavelength of the parasitic modes was smaller by a factor of two w.r.t. the theoretical predictions.

Motivated by this good agreement, we test in this paper further predictions of the parasitic model, especially those for the maximum amplification of the Maxwell stress by the MRI channel modes at termination. Two different termination criteria were

proposed within the parasitic model (PG09). Depending on the termination criterion used in their calculations, Latter et al. (2010) and Pessah (2010) obtained different estimates for the maximum magnetic field amplification. So far, these predictions have not been tested with direct numerical simulations.

In order to properly define the context in which this paper is written, we point out that the MRI represents only one way of field amplification in CCSNe besides mechanisms such as compression, linear winding of poloidal into toroidal field, and hydrodynamic instabilities such as convection and the standing accretion shock instability (SASI). The former two do not represent major numerical challenges and, hence, their effect on the field strength can be understood quite easily, whereas the complexity of the latter translates into a significant uncertainty in the factors by which the field is amplified with results ranging from a factor of about 5 (Obergaulinger et al. 2014) to several orders of magnitude (Endeve et al. 2010). Our work is not concerned with these processes, but solely focuses on the MRI, as our numerical methods are not directly suited to studying, e.g. the large-scale geometry of SASI modes. In this context, we should clearly state what we mean by magnetic field amplification, since there can be more than a single amplification stage. There is a primary magnetic field amplification resulting from the exponential field growth starting from the initial magnetic seed and ending when coherent MRI channels are disrupted, the field growth saturates and a turbulent state results. In the turbulent state, subsequent episodes of (secondary) MRI amplification may be driven, or a turbulent dynamo could be formed. In this work, we only concentrate on the primary magnetic field amplification, as a further discussion of the MRI turbulent state is beyond the scope of this paper.

As we have discussed in Rembiasz et al. (2016a), three dimensional (3D) *global* simulations to properly assess whether the MRI saturates when it begins from *realistically* (small) magnetic fields of prototypical massive stars are beyond the capacities of current supercomputers. Such simulations require a prohibitively large spatial numerical resolution. Furthermore, a two dimensional (2D) modelling of the saturation process of the MRI (in which axial symmetry is assumed for the stellar core) leads to qualitatively and quantitatively wrong results. In 2D the dominant non-axisymmetric KH modes are suppressed and the MRI is terminated by sub-dominant parasitic tearing modes. Consequently, 2D simulations overestimate the capability of the MRI to amplify the magnetic field (Rembiasz et al. 2016a). Hence, we are nowadays still forced to conduct our studies on this matter employing semi-global models as the ones we present here.

The aforementioned limitations of our method make it impossible for us to include possibly important effects such as global modes of the MRI and the interaction of the MRI with other instabilities. In light of these restrictions, our goal is to find an *upper limit* for the field amplification by the MRI channel modes by studying the *most favourable* conditions for these channel modes to develop.

As we will find that the amplification remains limited even under these optimal conditions, we can conclude that channel modes alone cannot lead to dynamically relevant field from weak initial fields. Other processes are therefore needed, such as for example an MRI-driven turbulent dynamo in the turbulent phase that follows channel mode disruption.

In Sec. 2 we describe the initial stage of the MRI during which channel modes develop. Next, we discuss its termination via the parasitic instabilities, examining two different physical termination criteria. Finally, we present some estimates for the maximum mag-

¹ Latter et al. (2009) classifies the types of parasitic modes differently.

netic field amplification based on the parasitic model. In Sec. 3, we describe two different numerical codes used in our studies and the initial setup of our 3D simulations. We present the results of these simulations in Sec. 4, and summarise our findings in Sec. 5.

2 MRI GROWTH AND TERMINATION

2.1 Physical model

We consider flows that can be described by the equations of resistive-viscous (non-ideal) magnetohydrodynamics (MHD). In the presence of an external gravitational potential, Φ , these equations read

$$\partial_t \rho + \nabla \cdot (\rho \mathbf{v}) = 0, \quad (1)$$

$$\partial_t (\rho \mathbf{v}) + \nabla \cdot (\rho \mathbf{v} \otimes \mathbf{v} + \mathbf{T}) = -\rho \nabla \Phi, \quad (2)$$

$$\partial_t e_\star + \nabla \cdot \left[e_\star \mathbf{v} + \mathbf{v} \cdot \mathbf{T} + \eta \left(\mathbf{b} \cdot \nabla \mathbf{b} - \frac{1}{2} \nabla \mathbf{b}^2 \right) \right] = -\rho \mathbf{v} \cdot \nabla \Phi, \quad (3)$$

$$\partial_t \mathbf{b} + \nabla \cdot (\mathbf{v} \otimes \mathbf{b} - \mathbf{b} \otimes \mathbf{v}) = \eta \nabla^2 \mathbf{b}, \quad (4)$$

$$\nabla \cdot \mathbf{b} = 0, \quad (5)$$

where \mathbf{v} , ρ , η , and $\mathbf{b} \equiv \mathbf{B} / \sqrt{4\pi}$ are the fluid velocity, the density, a uniform resistivity, and the redefined magnetic field \mathbf{B} , respectively. The total energy density, e_\star , is composed of fluid and magnetic contributions, i.e. $e_\star = \varepsilon + \frac{1}{2} \rho \mathbf{v}^2 + \frac{1}{2} \mathbf{b}^2$ with the internal energy density ε and the gas pressure $p = p(\rho, \varepsilon, \dots)$. The stress tensor \mathbf{T} is given by

$$\mathbf{T} = \left[P + \frac{1}{2} \mathbf{b}^2 + \rho \left(\frac{2}{3} \nu - \xi \right) \nabla \cdot \mathbf{v} \right] \mathbf{I} - \mathbf{b} \otimes \mathbf{b} - \rho \nu \left[\nabla \otimes \mathbf{v} + (\nabla \otimes \mathbf{v})^T \right], \quad (6)$$

where \mathbf{I} is the unit tensor, and ν and ξ are the kinematic shear and bulk viscosity, respectively.

2.2 Magnetorotational instability

We study the MRI in a small portion of the rotating star at a given distance r from the rotation axis, embedded in a magnetic field. For convenience, we use cylindrical coordinates (r, ϕ, z) , hereafter. We restrict our analysis to locations close to the equatorial plane ($z = 0$) and vertical perturbation wavevectors for which the MRI is known to develop fastest (see, e.g. Balbus & Hawley 1998). In this case, we can consider a differentially rotating fluid with angular frequency Ω and velocity

$$\mathbf{v} = \Omega r \hat{\phi}, \quad (7)$$

threaded by a uniform vertical magnetic field

$$\mathbf{b} = b_{0z} \hat{\mathbf{z}} \quad (8)$$

in the local perturbation analysis. Here, $\hat{\phi}$ and $\hat{\mathbf{z}}$ are the unit vectors in the direction ϕ and z , respectively. We assume an angular velocity with a radial dependence of the form

$$\Omega = \Omega_0 \left(\frac{r}{r_0} \right)^{-q}, \quad (9)$$

where Ω_0 is the angular velocity at the characteristic radius r_0 , and q is the local rotational shear given by

$$q = -\frac{d \ln \Omega}{d \ln r}. \quad (10)$$

Balbus & Hawley (1991) investigated the stability of such a system in the limit of linearised ideal MHD equations, and found

that it is unstable against modes, usually referred to as *MRI channels*, which grow exponentially with time. The most unstable MRI mode is characterised by the vertical wavevector

$$k_{\text{MRI}} = \sqrt{1 - \frac{(2-q)^2}{4}} \frac{\Omega}{c_{Az}}, \quad (11)$$

where $c_{Az} \equiv b_{0z} / \sqrt{\rho}$ is the Alfvén speed in the vertical direction, and grows at a rate

$$\gamma_{\text{MRI}} = \frac{q}{2} \Omega. \quad (12)$$

Its velocity and magnetic field are given by

$$\mathbf{v}_c(r, \phi, z, t) = \tilde{v}_c e^{\gamma_{\text{MRI}} t} (\hat{\mathbf{r}} \cos \phi_v + \hat{\phi} \sin \phi_v) \sin(k_{\text{MRI}} z), \quad (13)$$

$$\mathbf{b}_c(r, \phi, z, t) = \tilde{b}_c e^{\gamma_{\text{MRI}} t} (\hat{\mathbf{r}} \cos \phi_b + \hat{\phi} \sin \phi_b) \cos(k_{\text{MRI}} z), \quad (14)$$

where the subscript c stands for *channel*, $\hat{\mathbf{r}}$ is the unit vector in r direction, \tilde{v}_c and \tilde{b}_c are the initial amplitudes, ϕ_v and ϕ_b are the angles between the r -axis and the direction of the velocity and magnetic field channels, respectively. To simplify the notation, we define

$$v_c(t) = \tilde{v}_c e^{\gamma_{\text{MRI}} t}, \quad (15)$$

$$b_c(t) = \tilde{b}_c e^{\gamma_{\text{MRI}} t}, \quad (16)$$

and for brevity, we will often drop the explicit time dependence, i.e. $v_c = v_c(t)$ and $b_c = b_c(t)$. For the fastest-growing mode, the magnetic field and the velocity amplitudes are related by

$$v_c = \sqrt{\frac{q}{4-q}} c_{Ac}, \quad (17)$$

where $c_{Ac} \equiv b_c / \sqrt{\rho}$ is the Alfvén speed parallel to the MRI channel, and the channel angles are $\phi_v = \pi/4$ and $\phi_b = 3\pi/4$.

GX94 showed that MRI modes are exact solutions of the ideal incompressible MHD equations in the *shearing sheet* (local) approximation. This approximation consists in transforming the equations to a frame co-rotating with a fiducial fluid element and linearising the rotational profile around a radius r_0 , i.e. $\Omega(r) \approx (r - r_0) \partial_r \Omega(r)|_{r_0}$ (for a full description of this approximation, cf. Goldreich & Lynden-Bell 1965). Pessah & Chan (2008, PC08 hereafter) generalised the results of GX94 and showed that MRI channels (Eqs. 13 and 14) are also exact solutions of the resistive-viscous incompressible MHD equations in the shearing sheet approximation. They derived expressions for the growth rate, the amplitude ratio v_c/b_c , and the channel angles ϕ_v and ϕ_b of MRI-unstable modes for arbitrary hydrodynamic and magnetic Reynolds numbers defined as

$$R_e = \frac{c_{Az}^2}{\nu \Omega}, \quad (18)$$

$$R_m = \frac{c_{Az}^2}{\eta \Omega}. \quad (19)$$

Following PC08 and Rembiasz et al. (2016a), we use the same definitions of the Reynolds numbers. We note, however, that Guilet & Müller (2015), used a different definition of the Reynolds numbers, namely,

$$\tilde{R}_e = \frac{L_z^2 \Omega}{\nu}, \quad (20)$$

$$\tilde{R}_m = \frac{L_z^2 \Omega}{\eta}, \quad (21)$$

where L_z is the vertical size of the computational domain. We point out that assuming $L_z = \lambda_{\text{MRI}}$ and $q = 1.25$, which is the case in all simulations done with the code Snoopy presented in this paper (see

Sect. 3.1.2), those differently defined Reynolds numbers are related by

$$\tilde{R}_e = 46R_e, \quad (22)$$

$$\tilde{R}_m = 46R_m. \quad (23)$$

From now on, we will only use Reynolds numbers defined in Eqs. (18) and (19).

For the Reynolds numbers considered in our studies, i.e. $R_e, R_m \geq 100$, the characteristics of the fastest-growing MRI mode (i.e. its growth rate, wavelength, and angles) do not change by more than $\approx 2\%$ with respect to the ideal MHD case (PC08). We are therefore going to use Eqs. (11)–(17) in our farther analysis. For a more detailed discussion of non-ideal effects, we refer the reader to Rembiasz et al. (2016a).

2.3 MRI termination via parasitic instabilities

GX94 suggested that MRI channels may be unstable against parasitic instabilities, which could terminate the MRI growth. They found in their analytic calculations that in ideal MHD (shear driven) KH modes can develop on top of MRI channels. GX94 also suggested that in resistive MHD, parasitic instabilities of the (current driven) TM type could develop, too. Analytical calculations of Latter et al. (2009) in resistive MHD confirmed this hypothesis. Pessah (2010) extended these analytical studies to resistive-viscous MHD. He identified regions in parameter space, where depending on the values of the hydrodynamic and magnetic Reynolds numbers either KH or TM is the dominant (i.e. faster developing) secondary instability that terminates MRI growth. In particular, for the conditions prevailing in CCSNe outside of the neutrinosphere ($R_e, R_m \gg 1$) the exponential growth phase of the MRI should be terminated by KH instabilities. This hypothesis was confirmed with direct numerical simulations of Rembiasz et al. (2016a). In the remaining part of this subsection, we will first discuss the basic assumptions of the parasitic model then, we present some estimates which can be derived from it. A test of these predictions done with two different numerical codes will be presented in Sec. 4.

To compute the evolution of the parasitic instabilities, GX94 considered perturbations in a system with already well developed MRI channels given by

$$\mathbf{v} = -q\Omega_0(r - r_0)\hat{\phi} + \mathbf{v}_c(t) + \mathbf{v}_p(r, \phi, z, t), \quad (24)$$

$$\mathbf{b} = b_{0z}\hat{\mathbf{z}} + \mathbf{b}_c(t) + \mathbf{b}_p(r, \phi, z, t), \quad (25)$$

where \mathbf{v}_p and \mathbf{b}_p are the velocity and the magnetic field of the parasitic instabilities, respectively. Solving the equations governing the evolution of the secondary (parasitic) instabilities is a very challenging task, because MRI channels, which are treated as a background field for the perturbations, are non-stationary. Hence, standard analytical techniques cannot be used. To make this task more tractable for analytic studies, GX94 considered a stage of MRI growth when the amplitude of the MRI channels is much larger than the initial weak magnetic field, i.e. $b_c \gg b_{0z}$. The growth rate of the secondary instabilities γ_p (which scales $\propto b_c$) is then much larger than the MRI growth rate, i.e. $\gamma_p \gg \gamma_{\text{MRI}}$. Under these conditions the time evolution of the MRI channels, the Coriolis force, the background shear flow, and the initial background magnetic field b_{0z} can be neglected because they act on timescales comparable to γ_{MRI}^{-1} . Hence, instead of searching for solutions to perturbations according to Eqs. (24) and (25), GX94 considered a simplified system

where the velocity and the magnetic field are given by

$$\mathbf{v}(t) = \mathbf{v}_c(t_0) + \mathbf{v}_p(r, \phi, z, t), \quad (26)$$

$$\mathbf{b}(t) = \mathbf{b}_c(t_0) + \mathbf{b}_p(r, \phi, z, t), \quad (27)$$

with $t_0 = \text{const.}$ being the time at which the secondary perturbations are imposed. The same assumptions were also made in the studies of Latter et al. (2009), PG09 and Pessah (2010), even though these authors extrapolated their results to the regime in which $\gamma_p \sim \gamma_{\text{MRI}}$, in which case neglecting the above mentioned terms is not fully justified. Therefore, the analytical results obtained by Latter et al. (2009) and Pessah (2010) within the parasitic model can probably be improved, and direct numerical simulations should be used to test the former theoretical predictions.

In the ideal MHD limit, the dominant parasitic mode is of the KH type that develops along the MRI velocity channel (the projection of which in the horizontal plane, forms an angle 45° with respect to the radial direction in the anticlockwise sense) and is characterised by (e.g. Pessah 2010)

$$k_{\text{KH}} = 0.59k_{\text{MRI}} \quad (28)$$

and grows at a rate

$$\gamma_{\text{KH}} = 0.27k_{\text{MRI}}v_c. \quad (29)$$

Rembiasz et al. (2016a) observed in their numerical simulations that for $R_e, R_m \geq 100$ indeed the dominant parasitic modes are of the KH type and develop along the velocity channels. However, the wavelength of the parasitic modes was by a factor of two smaller than theoretically expected. As those authors did not investigate in detail the source of this discrepancy, the question whether it arises as a result of the numerics or truly from the underlying physics remains open.

2.3.1 Termination criteria

Since the MRI growth rate is constant in time (see Eq. (12)) and the growth rate of the KH instability grows exponentially with time (as $v_c \propto \exp(\gamma_{\text{MRI}}t)$), it is clear that at some point the latter will exceed the former, i.e. $\gamma_{\text{KH}} > \gamma_{\text{MRI}}$. Ultimately, the parasitic instabilities will therefore start to drain more energy from the MRI channels than the MRI can feed into them. This should eventually lead to the channel disruption (GX94).

PG09 proposed that the MRI is terminated at the time, t_t , when

$$\gamma_{\text{KH}}(t_t) = \gamma_{\text{MRI}} \quad (\text{termination criterion I}), \quad (30)$$

According to this criterion, by comparing Eq. (29) with Eq. (12) (and with the help of Eqs. 11 and 17), one can find that (independently of the value of q)

$$\frac{b_c(t_t)}{b_{0z}} = 3.8. \quad (31)$$

PG09 also suggested an alternative termination criterion, i.e. that it happens when the amplitudes of the MRI channels and parasitic modes are comparable, that is

$$v_p(t_t) = v_c(t_t) \quad \text{or} \quad (32)$$

$$b_p(t_t) = b_c(t_t) \quad (\text{termination criterion II}), \quad (33)$$

where v_p and b_p are the amplitudes of the parasitic instabilities. However, they did not investigate this last criterion in more detail analytically, as in this regime the problem becomes non-linear. Nevertheless, as pointed out by Latter et al. (2010), the termination criterion II seems to be physically much better justified. Indeed, at

the stage when parasites grow at an equal rate as the MRI channels, but the amplitudes of the parasites are much smaller (because they have been growing at a lower rate than the MRI), they can be still treated as small terms that can be neglected. Therefore, they should be of no physical importance and, in particular, should not be able to quench the MRI growth. Using termination criterion II (and taking into account the influence of the background shear in an approximate way), Latter et al. (2010) estimated that the background shear could increase the termination amplitude to $b_c(t_i)/b_{0z} \sim 24\text{--}40$ (depending on the considered amplitude of the parasitic perturbations), which is a considerably larger value than that estimated using the termination criterion I (Eq. 31).

Summing up the theoretical estimates, we find, on the one hand, that termination criterion I most probably underestimates the amplification of the magnetic field at MRI termination. Nevertheless, it may serve as a proxy for termination since, as we shall see from our numerical models, within 2–3 MRI time scales (i.e. γ_{MRI}^{-1}) after the growth rates are equal, the MRI channels will be disrupted by the parasitic instabilities. On the other hand, in order to use the termination criterion II, by its own definition, we should not treat parasitic perturbations as small, linearising the equations in terms of them, which makes it difficult to provide analytic estimates with a more physically adequate condition for MRI termination. This is why numerical simulations are indispensable to test the predictions of the parasitic model.

2.3.2 Some estimates

We define the absolute value of the volume-averaged Maxwell stress component as

$$\mathcal{M}_{r\phi} \equiv \frac{|\int b_r b_\phi dV|}{V}, \quad (34)$$

where V is the volume of the computational domain, and the amplification factor as

$$\mathcal{A} \equiv \frac{\sqrt{\mathcal{M}_{r\phi}^{\text{term}}}}{b_{0z}}, \quad (35)$$

where $\mathcal{M}_{r\phi}^{\text{term}} \equiv \mathcal{M}_{r\phi}(t_i)$. Assuming that at termination, the MRI channels are still given by Eq. (14) (i.e. undistorted) and ignoring the contribution of the parasitic instabilities, the Maxwell stress is

$$\mathcal{M}_{r\phi}^{\text{term}} = \frac{b_c^2(t_i)}{4}. \quad (36)$$

Hence, from the estimate done by PG09 using the termination criterion I (Eq. 31), we obtain

$$\mathcal{A} = 1.9. \quad (37)$$

Next, we want to make some estimates of the MRI termination amplitude within the parasitic model using the second termination criterion (Eq. 32). Note that we begin our analysis from the equations obtained by Pessah (2010) under some simplifying assumptions and that we will further introduce additional simplifications. Therefore, our estimates must be tested with the simulation results presented in Sec. 4.

In order to make use of the second termination criterion, we need to first find the time evolution of the parasitic KH modes. For this purpose, we assume that during their whole evolution, i.e. from their onset until the MRI termination, they can be factored in the following terms

$$\mathbf{v}_{\text{KH}}(r, \theta, z, t) = v_{\text{KH}}(t) \mathbf{f}_{\text{KH}}(r, \theta, z), \quad (38)$$

where $v_{\text{KH}}(t)$ is the instability amplitude and includes the time evolution of the perturbation, and \mathbf{f}_{KH} is a normalised function (i.e. $\max(\mathbf{f}_{\text{KH}}) = 1$) that does not depend on time (its explicit form can be found in Pessah 2010). Note that the factorisation assumed in Eq. (38) may fail because, among other reasons, (i) we neglect effects proportional to Ω (the shear and the Coriolis force), and (ii) because shortly before the MRI termination, when $v_{\text{KH}} \approx v_c$, the KH instability will enter the non-linear phase of its evolution. In this phase the KH perturbations eventually become comparable to the background shear, and the growth of the instability is reduced before its final termination (cf. Keppens et al. 1999; Obergaulinger et al. 2010).

We can find the time evolution of $v_{\text{KH}}(t)$ from the definition of the KH instability growth rate, i.e.

$$\gamma_{\text{KH}}(t) \equiv \frac{\dot{v}_{\text{KH}}(t)}{v_{\text{KH}}(t)}, \quad (39)$$

provided that $\gamma_{\text{KH}}(t)$ is known. The resulting differential equation can be integrated analytically if we assume $\gamma_{\text{KH}}(t) = \sigma k_{\text{MRI}} v_c(t)$, where $\sigma = \text{const.}^2$, that is (see Latter 2016, for a similar calculation on a different primary instability)

$$v_{\text{KH}}(t) = v_{\text{KH}}(t_0) \exp \left[\frac{\sigma k_{\text{MRI}} v_c(t_0)}{\gamma_{\text{MRI}}} (e^{\gamma_{\text{MRI}} t} - e^{\gamma_{\text{MRI}} t_0}) \right], \quad (40)$$

where t_0 is the time at which the KH perturbations begin to grow. Assuming $t_0 = 0$, we finally obtain

$$v_{\text{KH}}(t) = \tilde{v}_{\text{KH}} \exp \left[\frac{\sigma k_{\text{MRI}} \tilde{v}_c}{\gamma_{\text{MRI}}} (e^{\gamma_{\text{MRI}} t} - 1) \right], \quad (41)$$

where \tilde{v}_{KH} is the initial KH amplitude.

Now, we can determine the MRI termination amplitude from the condition

$$\frac{v_{\text{KH}}(t_i)}{v_c(t_i)} = s, \quad (42)$$

where for $s = 1$, we recover the termination criterion II exactly, but we allow this parameter to slightly vary, as the choice $s = 1$ is somewhat arbitrary. With the help of Eqs. (15) and (41), we can rewrite the above condition as

$$\tilde{v}_{\text{KH}} e^{\gamma_{\text{MRI}} t_i} = \frac{\gamma_{\text{MRI}}}{\sigma k_{\text{MRI}}} \left[\ln \left(\frac{s \tilde{v}_c}{\tilde{v}_{\text{KH}}} \right) + \gamma_{\text{MRI}} t_i \right] + \tilde{v}_c \quad (43)$$

where the term on the LHS of Eq. (43) is equal to the definition of the velocity amplitude at termination $v_c(t_i)$ (see, Eq. 15).

We note that Eq. (43) should be treated as an equation for t_i . There is a trivial solution, $t_i = 0$, for $\tilde{v}_{\text{KH}} = s \tilde{v}_c$. However, these are not physically plausible initial conditions. For the MRI channels to be destroyed by the KH instability, they should exist in the first place. So even if we start with completely random initial perturbations (which is physically plausible), we first expect the MRI channels to develop, implying that $t_i > 0$. Then, after a sufficiently developed velocity shear sets in between the channels, the parts of the initial perturbations which do not promote the growth of the MRI will seed the growth of the KH instabilities. In practical terms, this means that we can safely assume that $\tilde{v}_{\text{KH}} < s \tilde{v}_c$ ($s \lesssim 1$). From Eqs. (17) and (36), we find

$$v_c(t_i) = \sqrt{\frac{4q}{4-q}} \mathcal{A} c_{\text{Az}}. \quad (44)$$

² For $\sigma = 0.27$, we recover Eq. (29), however for the time being we want to use a bit more general expression.

Comparing Eq. (44) with Eq. (43), we obtain

$$\mathcal{A} = \frac{1}{2\sigma} \left[\ln \left(\frac{s\tilde{v}_c}{\tilde{v}_{KH}} \right) + \gamma_{MRI} t_t \right] + \sqrt{\frac{4-q}{4q}} \frac{\tilde{v}_c}{c_{Az}}, \quad (45)$$

where we also used Eqs. (11) and (12). From Eqs. (15), evaluated at $t = t_t$, and (44), we find

$$\gamma_{MRI} t = \ln \left(\sqrt{\frac{4q}{4-q}} \mathcal{A} \frac{c_{Az}}{\tilde{v}_c} \right) \quad (46)$$

that we substitute into Eq. (45), to finally obtain

$$\mathcal{A} - \frac{1}{2\sigma} \ln \mathcal{A} = \frac{1}{2\sigma} \left[\ln \left(\frac{c_{Az}}{\tilde{v}_{KH}} \right) + \ln \left(s \sqrt{\frac{4q}{4-q}} \right) \right] + \sqrt{\frac{4-q}{4q}} \frac{\tilde{v}_c}{c_{Az}}. \quad (47)$$

Since, typically $\tilde{v}_c/c_{Az} \ll 1$ and $c_{Az}/\tilde{v}_{KH} \gg 1$, the amplification factor should be almost independent of the initial MRI channel amplitude and depend logarithmically on the ratio of the initial velocity amplitude of the parasitic instabilities to the amplitude of the background Alfvén speed (or, equivalently, the initial magnetic field strength). For $\sigma = 0.27$ (the value calculated by PG09), $s = 1$ and $c_{Az}/\tilde{v}_{KH} = 1000$ (a typical value used in our simulations), we obtain

$$\mathcal{A} \simeq 19. \quad (48)$$

Finally, we discuss the results of Latter et al. (2010) who gave an approximate description of the influence of the background shear on the development of the parasitic instabilities. They pointed out that due to shear, the radial wavenumber of non-axisymmetric parasitic modes increases linearly with time while the azimuthal wavenumber remains unchanged. As a consequence, during most of its evolution, the parasitic mode is expected to grow at a rate smaller than that predicted by GX94, since its wavelength and orientation w.r.t. the velocity channel is not optimal. Moreover, the parasitic mode can only grow for a limited time τ before the shear prevents its further growth completely. Latter et al. (2010) found that the dominant mode would have at most a time of

$$\tau = \frac{2.18}{q\Omega} \quad (49)$$

for its development. Furthermore, they roughly estimated that the growth rate of the mode is reduced by a factor of two as a result of the shear, i.e.

$$\gamma_{KH}(t) = \frac{\sigma}{2} k_{MRI} v_c(t), \quad (50)$$

and calculated the MRI termination amplitude, from the condition (42) assuming that parasitic perturbations are introduced at $t = t_0 \neq 0$ and that $\tau = t_t - t_0$. If within the time interval τ , condition (42) is not met, the MRI will not be terminated. Hence, these authors determined the minimum amplitude of the velocity perturbations $v_c(t_0)$ for which the parasitic modes can catch up with the MRI channels after the aforementioned time interval τ has passed. When calculating the growth rate of the parasitic instabilities, Latter et al. (2010) further neglected the fact that within the time interval τ the parasitic growth rate increases as the MRI channel amplitude increases with time. They thus obtain

$$v_{KH}(t) = v_{KH}(t_0) \exp \left[\frac{\sigma}{2} k_{MRI} v_c(t_0) (t - t_0) \right]. \quad (51)$$

By plugging Eq. (51) to Eq. (42), we have

$$\frac{v_{KH}(t_0)}{v_c(t_0)} \exp \left[\tau \left(\frac{\sigma}{2} k_{MRI} v_c(t_0) - \gamma_{MRI} \right) \right] = s, \quad (52)$$

from which we can calculate (using also Eqs. 11, 12 and 17)

$$\mathcal{A} = \frac{1}{\sigma} \left[0.92 \ln \left(\frac{sv_c(t_0)}{v_{KH}(t_0)} \right) + 1 \right]. \quad (53)$$

In order to make a further progress with this equation, we have to calculate $v_{KH}(t_0)$, $(v_c(t_0) = \tilde{v}_c e^{\gamma_{MRI} t_0})$ from Eq. (15). By assuming that growth of the parasitic instabilities from time $t = 0$ to $t = t_0$ is negligible, i.e. $v_{KH}(t_0) \approx v_{KH}(0) = \tilde{v}_{KH}$, which is well justified in the light of our simulations done with Snoopy (see Fig. 4.1.2 of model #S19 discussed in Sec. 2), we finally obtain

$$\mathcal{A} - \frac{0.92}{\sigma} \ln \mathcal{A} = \frac{0.92}{\sigma} \left[\ln \left(\frac{c_{Az}}{\tilde{v}_{KH}} \right) + \ln \left(s \sqrt{\frac{4q}{4-q}} \right) \right] + \frac{1}{\sigma}. \quad (54)$$

This equation has a very similar form to Eq. 47, but predicts larger amplification factors by a factor ≈ 2 . For typical values used in our simulations (see the discussion above Eq. 48), we obtain

$$\mathcal{A} \simeq 41. \quad (55)$$

Note, however, that as in Latter et al. (2010), it was assumed that $b_c(t_i) \approx b_c(t_0)$, i.e. the growth of the magnetic field in the time interval τ was neglected. Taking this effect into account would increase the estimate of \mathcal{A} by another factor of $\exp(\gamma_{MRI} \tau) \approx 3$, i.e.

$$\mathcal{A} \simeq 123. \quad (56)$$

3 NUMERICAL SETUP

To test the predictions of the parasitic model, we perform simulations using two different numerical codes, a finite-volume code, AENUS, and a pseudo-spectral code, SNOOPY, that we describe briefly in the following subsections. The advantages and disadvantages of the simulations performed with these codes will be discussed in Sec. 4.

3.1 Numerical codes

3.1.1 Aenus

We use the three-dimensional Eulerian MHD code AENUS (Obergaullinger 2008) to solve the MHD equations (1)–(5). The code is based on a flux-conservative, finite-volume formulation of the MHD equations and the constrained-transport scheme to maintain a divergence-free magnetic field (Evans & Hawley 1988). The code is based on high-resolution shock-capturing methods (e.g. LeVeque 1992). It implements various optional high-order reconstruction algorithms, including a total-variation-diminishing piecewise-linear (TVD-PL) reconstruction of second-order accuracy, a third-, fifth-, seventh- and ninth-order monotonicity-preserving (MP3, MP5, MP7 and MP9, respectively) scheme (Suresh & Huynh 1997), a fourth-order, weighted, essentially non-oscillatory (WENO4) scheme (Levy et al. 2002), and approximate Riemann solvers based on the multi-stage (MUSTA) method (Toro & Titarev 2006). We add terms including viscosity and resistivity to the flux terms in the Euler equations and to the electric field in the MHD induction equation. We treat these terms similarly to the fluxes and electric fields of ideal MHD. The derivatives of velocity and magnetic field appearing in the viscous fluxes and resistive electric field, respectively, are computed from reconstructed states obtained by same high-order reconstruction methods as for the terms of ideal MHD. The explicit time integration can be done with Runge-Kutta schemes of first, second, third, and fourth order (RK1, RK2, RK3, and RK4), respectively.

We performed the simulations reported here with the MP9 scheme, a MUSTA solver based on the HLLD Riemann solver, and an RK3 time integrator (Harten 1983; Miyoshi & Kusano 2005). See Rembiasz et al. (2016a) for a justification of this choice.

3.1.2 Snoopy

We use the pseudo-spectral code SNOOPY (Lesur & Longaretti 2005, 2007) to solve the MHD equations (1)–(5) in the shearing box and incompressible approximations. The incompressible approximation holds if both the flow and Alfvén velocities are much less than the sound speed. It further assumes a uniform background density ρ_0 and entropy, i.e. one neglects the radial density and entropy gradients. The incompressible approximation can be considered a special case of the Boussinesq approximation (when the entropy gradient vanishes), whose validity in the CCSN conditions has been extensively discussed in Guilet & Müller (2015). SNOOPY solves the 3D shearing box equations using a spectral Fourier method, where the shear is handled through the use of a shearing wave decomposition (with time varying radial wavevector) and a periodic remap procedure. Nonlinear terms are computed with a pseudo-spectral method using the 2/3 dealiasing rule. The time integration is performed using an implicit procedure for the diffusive terms, while other terms use an explicit 3rd order Runge Kutta scheme. SNOOPY is parallelised using both MPI and OpenMP techniques. It has been extensively used in the past to study the MRI in the context of accretion discs (Lesur & Longaretti 2007; Longaretti & Lesur 2010; Rempel et al. 2010; Lesur & Longaretti 2011; Meheut et al. 2015; Walker et al. 2015) and PNSs (Guilet & Müller 2015).

3.1.3 Initial conditions

In the simulations performed with AENUS, following Rembiasz et al. (2016a) and Obergaulinger et al. (2009), we use equilibrium initial conditions based on the final stages of post-bounce cores from Obergaulinger et al. (2006a), in which (several tens of milliseconds after core bounce) the shock wave has reached distances of a few hundred kilometres and the post-shock region exhibits a series of damped oscillations as the PNS relaxes into a nearly hydrostatic configuration. The rotational profile (given by Eq. 9 with $\Omega_0 = 767 \text{ s}^{-1}$, and $q = 1.25$) that we used in our simulations, is similar to the one employed in the global MRI simulations of Obergaulinger et al. (2006a). Because the resulting centrifugal force is insufficient to balance gravity, the gas is kept in (an initial hydrodynamic) equilibrium by an additional pressure gradient, so that

$$\rho \partial_r \Phi - \partial_r P + r \rho \Omega^2 = 0. \quad (57)$$

The initial distributions of angular velocity, density, and gravitational potential were obtained by rescaling those used by Rembiasz et al. (2016a, Fig. 1) to match the conditions encountered at the PNS surface (see Appendix A for more details).

At this location, neutrinos do not have a strong impact on the dynamics (Guilet et al. 2015) and we therefore expect a very small viscosity. In all AENUS simulations (see Tab. 1), we set the shear and bulk viscosity to $\nu = \xi = 0 \text{ cm}^2 \text{ s}^{-1}$, and the value of resistivity was chosen so that the magnetic Reynolds number $R_m = 100$. Therefore, if we consider, e.g. an initial magnetic field strength $b_{0z} = 1.22 \times 10^{13} \text{ G}$, the previous value of R_m corresponds to $\eta = 7.48 \times 10^8 \text{ cm}^2 \text{ s}^{-1}$. The typical simulation domain was set to $L_r \times L_\phi \times L_z = 2 \text{ km} \times 2 \text{ km} \times \lambda_{\text{MRI}}$, except for the models #A7, #A8a,b,c, #A11, in which $L_r \times L_\phi \times L_z = 2 \text{ km} \times 8 \text{ km} \times 3\lambda_{\text{MRI}}$. Note

however, that both R_m and λ_{MRI} are not constant in the computational domain but vary by some $\approx 20\%$ (see Rembiasz et al. 2016a, for details).

We assume periodic boundary conditions in the directions ϕ and z . In the radial direction, we use shearing disc boundary conditions (Klahr & Bodenheimer 2003), i.e. we apply periodic boundary conditions to the deviation of several variables from their initial state. For instance, applied to the fluid density we have that such deviation is

$$\delta\rho(r, t) \equiv \rho(r, t) - \rho(r, 0), \quad (58)$$

and we enforce shear-periodicity of the variables $\delta\rho(r, t)$ (see Rembiasz et al. 2016a, for a more detailed justification of this choice). We apply these boundary conditions to angular velocity, density, momentum, and entropy. Because the initial magnetic field is homogeneous in all our simulations, we use periodic boundary conditions for this quantity too.

In all SNOOPY simulations (see Tab. 2), we use analogous initial conditions with the exceptions that simulations are done in the frame corotating with the fluid and the rotational profile is linearised (shearing box approximation). Moreover, the background density is uniform and set to $\rho_0 = 2.47 \times 10^{12} \text{ g cm}^{-3}$ (which corresponds to the central value in AENUS simulations), and the shear viscosity and resistivity are chosen so that $R_e = R_m = 100$.

In the simulations done with AENUS, following Rembiasz et al. (2016a), to trigger the MRI we impose an initial velocity perturbation on the background velocity profile (defined by Eq. 7) of the form

$$\mathbf{v}_1 = \Omega r [\{\delta_r \mathfrak{R}_r(r, \phi, z) + \epsilon \sin(k_z z)\} \hat{\mathbf{r}} + \delta \mathfrak{R}_\phi(r, \phi, z) \hat{\boldsymbol{\phi}} + \delta \mathfrak{R}_z(r, \phi, z) \hat{\mathbf{z}}], \quad (59)$$

where $\mathfrak{R}_r(r, \phi, z)$, $\mathfrak{R}_\phi(r, \phi, z)$, and $\mathfrak{R}_z(r, \phi, z)$ are random numbers in the range $[-1, 1]$, δ and δ_r are the perturbation amplitudes, k_z is the vertical perturbation wavenumber, and ϵ is the amplitude of the sinusoidal perturbation in the z -direction. We choose $\delta_r = 0.1\delta$. Typically, ϵ and δ are of the order of 10^{-5} . Their exact values in each simulation can be found in Tab. 1.

The random perturbations added to the channel modes in our simulations are rather small compared with the actual perturbations (of the order of one) expected in the collapsed core of a massive star. Larger perturbations result in shorter periods of magnetic field growth by the action of MRI channels. Thus, we expect that our numerical results set an upper bound for the field amplification by MRI channels in the collapsed core of massive stars.

In all simulations we set $k_z = k_{\text{MRI}}$, with the only exception being model #A9b in which $k_z = 3k_{\text{MRI}}$. Even though we initialise the channel only in one velocity component instead of both radial and azimuthal components of velocity and magnetic field, the other components quickly grow and form a fully developed channel mode.

In SNOOPY simulations, we use five different prescriptions for the initial perturbations. In simulations #S1a–#S18 from Tab. 2, to the background velocity, $\mathbf{v}_0 = -q\Omega_0(r - r_0)\hat{\boldsymbol{\phi}}$, we added “one component of an MRI channel”, i.e.

$$\mathbf{v}_\epsilon = \epsilon \Omega_0 r_0 \hat{\mathbf{r}} \sin(k_{\text{MRI}} z) \quad (60)$$

and random perturbations of the form

$$\tilde{\mathbf{v}}_1 = \delta \Omega_0 r_0 \sum_{\beta} \hat{\boldsymbol{\beta}} \sum_{l,m,n} \mathfrak{R}_{\beta}^{lmn} \sin(k_l r + k_m \phi + k_n z + \chi_{\beta}^{lmn}) \quad (61)$$

where $\beta \in \{r, \phi, z\}$, $k_\beta = 2\pi l/L_\beta$, \mathfrak{R}_{lmn} and χ_{lmn} are random amplitude and phase of a given mode. The sum is restricted to Fourier

modes with wavelength longer than 0.1 km. The amplitudes \mathfrak{R}_β^{lmn} are random numbers between 0 and $\delta\Omega_0 r_0 / \sqrt{n_{\text{pert}}}$, where n_{pert} is the number of excited modes. The solenoidal nature of the velocity field in the incompressible approximation is enforced *a posteriori* by subtracting the divergence part of the field. Random magnetic field perturbations \mathbf{b}_1 are constructed in an analogous way, the Alfvén velocity replacing the velocity in the equations. Hence the final form of the initial velocity and magnetic field is

$$\mathbf{v} = -q\Omega_0(r - r_0)\hat{\phi} + \mathbf{v}_c + \tilde{\mathbf{v}}_1, \quad (62)$$

$$\mathbf{b} = b_{0c}\hat{\mathbf{z}} + \mathbf{b}_1. \quad (63)$$

The values of δ and ϵ in each simulation can be found in Tab. 2. The perturbations in simulations #S19 follow from the same procedure except that all wavelengths down to the grid scale are perturbed. In simulations #SA15a–e from Tab. 2 the random velocity perturbations $\tilde{\mathbf{v}}_1$ are replaced by cell-by-cell random values in the range $[-\delta r_0\Omega_0, \delta r_0\Omega_0]$ for each velocity component, while the magnetic field perturbations vanish $\tilde{\mathbf{b}}_1 = 0$.

In simulations #SCA15a–#SCA16c and #SCR15a–c from Tab. 4, the initial velocity and magnetic field are given by

$$\mathbf{v} = -q\Omega_0(r - r_0)\hat{\phi} + \mathbf{v}_c + \tilde{\mathbf{v}}_1, \quad (64)$$

$$\mathbf{b} = b_{0c}\hat{\mathbf{z}} + \mathbf{b}_c + \mathbf{b}_1, \quad (65)$$

where \mathbf{v}_c and \mathbf{b}_c are the full channel mode solution given by Eqs. (13) and (14), respectively, and $\tilde{\mathbf{v}}_c = \epsilon\Omega_0 r_0$ and $\tilde{\mathbf{b}}_c$ is determined from Eq. (17). In simulations #SCR15a–c random perturbations $\tilde{\mathbf{v}}_1$ and $\tilde{\mathbf{b}}_1$ follow equation (61) as explained above, whereas in simulations #SCA15a–#SCA16c they are replaced by cell-by-cell random values for the velocity and zero magnetic field perturbation.

Rembiasz et al. (2016a) comprehensively studied the influence of the geometry of the computational domain, i.e. its aspect ratio both in the vertical and azimuthal direction, on the magnetic field amplification. Based on these studies, we have chosen computational boxes in such a way as to not affect the MRI termination amplitude.

4 RESULTS

4.1 Termination criterion

The goal of this section is to determine which termination criterion (I or II, Eqs. 30 and 32, respectively) is a better predictor for the MRI termination. To this end, we analyse in detail simulations #A8a (which was also presented in Rembiasz et al. 2016a, as model #7, see Appendix A, for details) and #S19 performed with AENUS and SNOOPY, respectively.

4.1.1 Aenus simulation

We have calculated spatial discrete 3D Fourier transforms of the magnetic field, velocity and $\mathbf{w} \equiv \sqrt{\rho}\mathbf{v}$ components b_β , v_β , and w_β , respectively, with $\beta \in \{r, \phi, z\}$ at a given time using a Fast Fourier Transform (FFT) algorithm. We denote the complex FFT coefficients with \hat{b}_β , \hat{v}_β and \hat{w}_β , respectively. The power spectral density of the magnetic field is proportional to $|\hat{b}_\beta|^2$, which is a measure of the average magnetic field energy density of the component b_β in Fourier space. Analogously, the kinetic energy density is proportional to $|\hat{w}_\beta|^2$. We expect that MRI channel flows appear as structures with a wavevector

$$\mathbf{k}_{\text{MRI}} = (0, 0, k_{\text{MRI}}), \quad (66)$$

and the parasitic instabilities develop with non-zero radial and azimuthal wavenumbers.

The average magnetic and kinetic energy density of the field components b_β and w_β can be computed from the Fourier amplitudes as

$$e_\beta^{\text{mag}} = \frac{1}{2} \sum_{l=-N_r/2}^{N_r/2} \sum_{m=-N_\phi/2}^{N_\phi/2} \sum_{n=-N_z/2}^{N_z/2} |\hat{b}_\beta(k_l, k_m, k_n)|^2 \quad \text{and} \quad (67)$$

$$e_\beta^{\text{kin}} = \frac{1}{2} \sum_{l=-N_r/2}^{N_r/2} \sum_{m=-N_\phi/2}^{N_\phi/2} \sum_{n=-N_z/2}^{N_z/2} |\hat{w}_\beta(k_l, k_m, k_n)|^2, \quad (68)$$

where

$$(k_l, k_m, k_n) = \left(\frac{2\pi l}{L_r}, \frac{2\pi m}{L_\phi}, \frac{2\pi n}{L_z} \right). \quad (69)$$

We can estimate the average magnetic energy density of the MRI channels restricting the summation to locations in Fourier space relevant for this instability, i.e.

$$e_{\text{MRI},\alpha}^{\text{mag}} = |\hat{b}_\alpha(0, 0, k_{\text{MRI}})|^2, \quad (70)$$

$$e_{\text{MRI},\alpha}^{\text{kin}} = |\hat{w}_\alpha(0, 0, k_{\text{MRI}})|^2, \quad (71)$$

where here and in the following the subscript α is restricted to $\alpha \in \{r, \phi\}$.

To determine the horizontal component of the wavevector of the parasitic instabilities, Rembiasz et al. (2016a) analysed Fourier modes of b_α with finite k_r and k_ϕ , but $k_z = 0$. They found that the parasitic instabilities produce a characteristic signature with wavevectors $\mathbf{k}_p = (k_r, k_\phi, 0)$, where $k_r \simeq k_\phi \simeq 0.8k_{\text{MRI}}$. This means that in accordance with the parasitic model, parasitic instabilities develop along the velocity channels.

In this paper, we want to find an estimator for the total magnetic and kinetic energy stored in the parasitic instabilities. It is clear however, that the parasites will also contribute to other Fourier modes. For instance, according to Pessah (2010), the dominant parasitic mode will contribute to all Fourier modes with $\mathbf{k}_p = (\zeta k_{\text{MRI}}, \zeta k_{\text{MRI}}, n k_{\text{MRI}})$, where $\zeta = 0.42$ and n is a natural number. However, we expect to see not only the dominant modes in our simulations. Moreover, as pointed out by Latter et al. (2010), PG09 and Pessah (2010) the rotational shear will modify the horizontal components of the parasitic modes (making them time dependent). Thus, we take

$$e_{p,\beta}^{\text{mag}} = e_\beta^{\text{mag}} - \frac{1}{2} \sum_{l=-N_r/2}^{N_r/2} \sum_{n=-N_z/2}^{N_z/2} |\hat{b}_\beta(k_l, 0, k_n)|^2 \quad (72)$$

$$e_{p,\beta}^{\text{kin}} = e_\beta^{\text{kin}} - \frac{1}{2} \sum_{l=-N_r/2}^{N_r/2} \sum_{n=-N_z/2}^{N_z/2} |\hat{w}_\beta(k_l, 0, k_n)|^2, \quad (73)$$

as an estimator for the energy stored in parasitic modes, i.e. we take all Fourier modes but the axisymmetric ones.

Figure 1 (upper panels) shows the time evolution of the magnetic and kinetic energy density for both the MRI and the parasitic instabilities (given by Eqs. 70–73; see Fig. 2 for the corresponding results of a SNOOPY simulation). The MRI (Fourier) modes grow exponentially with time at a constant rate from $t \approx 8$ ms to $t \approx 24$ ms. The average magnetic and kinetic energy density $e_{p,\alpha}^{\text{mag}}$ and $e_{p,\alpha}^{\text{kin}}$, respectively, of the parasites begin to grow super-exponentially at $t \approx 20$ ms from a value of about 6 orders of magnitude smaller than that of the MRI. According to termination criterion I, the MRI termination should occur already at $t \approx 21$ ms (see bottom panels of Fig. 1) however, we observe that the MRI keeps growing for ~ 5 ms ($\sim 2.7 \gamma_{\text{MRI}}^{-1}$) longer until the amplitude of the parasitic

Table 1. Overview of our 3D MRI simulations done with AENUS. The columns give the model identifier, the magnetic field strength, the hydrodynamic and magnetic Reynolds numbers (R_e and R_m , respectively), MRI wavelength, λ_{MRI} , the size of the computational domain, the resolution, the number of grid cells per MRI wavelength, initial perturbation amplitudes ϵ and δ (see Eq. 59), the volume-averaged Maxwell stress (Eq. 34) at termination, and the amplification factor (Eq. 35).

#	b_{0z} [10^{13} G]	R_e	R_m	λ_{MRI} [km]	box size ($r \times \phi \times z$) [km]	resolution ($r \times \phi \times z$)	zones per channel	$\epsilon[10^{-5}]$	$\delta[10^{-5}]$	$\mathcal{M}_{r\phi}^{\text{term}}$ [10^{28} G ²]	\mathcal{A}
A1	0.73	∞	100	0.4	$2 \times 2 \times 0.4$	$100 \times 100 \times 20$	20	0.2	1	3.3	24.8
A2	0.73	∞	100	0.4	$2 \times 2 \times 0.4$	$168 \times 168 \times 34$	34	0.2	1	2.6	22.2
A3	0.73	∞	100	0.4	$2 \times 2 \times 0.4$	$336 \times 336 \times 68$	68	0.2	1	2.5	21.4
A4	0.73	∞	100	0.4	$2 \times 2 \times 0.4$	$672 \times 672 \times 136$	136	0.2	1	2.5	21.3
A5	0.92	∞	100	0.5	$2 \times 2 \times 0.5$	$136 \times 136 \times 34$	34	0.2	1	3.5	20.3
A6	0.92	∞	100	0.5	$2 \times 2 \times 0.5$	$272 \times 272 \times 68$	68	0.2	1	3.4	20.0
A7	1.22	∞	100	0.666	$2 \times 8 \times 2$	$60 \times 240 \times 60$	20	0.2	1	7.8	22.9
A8a	1.22	∞	100	0.666	$2 \times 8 \times 2$	$100 \times 400 \times 100$	33	0.2	1	6.6	21.0
A8b	1.22	∞	100	0.666	$2 \times 8 \times 2$	$100 \times 400 \times 100$	33	0.2	1	6.6	21.0
A8c	1.22	∞	100	0.666	$2 \times 8 \times 2$	$100 \times 400 \times 100$	33	0.2	1	6.6	21.1
A9a	1.22	∞	100	0.666	$2 \times 2 \times 0.666$	$100 \times 100 \times 34$	34	0.2	1	6.6	21.0
A9b	1.22	∞	100	0.666	$2 \times 2 \times 0.666$	$100 \times 100 \times 34$	34	0.2	1	6.0	20.0
A10	1.22	∞	100	0.666	$2 \times 8 \times 2$	$200 \times 800 \times 200$	67	0.2	1	5.2	18.6
A11	1.22	∞	100	0.666	$2 \times 2 \times 0.666$	$400 \times 400 \times 134$	134	0.2	1	5.2	18.6

* λ_{MRI} , R_e and R_m are not constant in the computational domain, but vary by $\approx 20\%$ (see Rembiasz et al. 2016a, for a discussion).

** $R_e = \infty$ means that the only viscosity present in the models is of numerical origin. The numerical viscosity of the code is discussed in Rembiasz (2013).

modes becomes comparable to the amplitude of the MRI (upper panels of Fig. 1). Therefore, we conclude that termination criterion II provides a better proxy for the termination of the MRI growth.

We finally note that the time interval between the fulfillment of the termination criterion I and MRI termination, $\sim 2.7\gamma_{\text{MRI}}^{-1}$, can be somewhat reduced by the contamination caused by the boundary conditions used in AENUS simulations (see also Sec. 4.1.2, where for an analogous SNOOPY simulation, this time interval is $\approx 3\gamma_{\text{MRI}}^{-1}$). In Appendix B, we discuss in more detail the influence of the boundary conditions used in AENUS simulations, as well as we make a more detailed comparison of AENUS and SNOOPY simulations.

4.1.2 Snoopy simulation

We repeat an analogous analysis of simulation #S19 done with SNOOPY. Figure 2 shows the time evolution of the magnetic and kinetic energy density for both the MRI and the parasitic instabilities (given by Eqs. 70–73). The MRI (Fourier) modes grow exponentially with time at a constant rate from $t \approx 8$ ms to $t \approx 27$ ms. Like in the AENUS simulation, the parasitic instabilities growth rate increases with the MRI amplitude in agreement with theoretical expectations. An interesting feature that appears in the SNOOPY simulation is that the growth rate of the parasitic modes shows oscillations with time with a period $\tau \approx 2$ –3 ms (bottom panels of Fig. 2). These oscillations could be caused by shear, as argued by Latter et al. (2010). A parasitic mode wavevector has the optimal orientation only for a limited time before its radial component becomes too large for an efficient growth. Note that according to Eq. (49), we would expect in this simulation $\tau = 2.27$ ms, which agrees very well with the observed period of the oscillations. This seems to hint that any future parasitic model should take the influence of the shear into account, as its influence on the parasitic modes is non-negligible.

The growth rate of parasitic instabilities reaches the growth rate of the MRI at $t \approx 23$ ms (termination criterion I; bottom panels

of Fig. 2). However, termination occurs only about 6 ms ($\approx 3\gamma_{\text{MRI}}^{-1}$) later when the amplitude of the parasitic modes becomes comparable to that of the MRI (termination criterion II; upper panels of Fig. 2). At $t \approx 25$ ms, both, the average magnetic energy density $e_{p,\alpha}^{\text{mag}}$ and the kinetic energy density $e_{p,\alpha}^{\text{kin}}$ of the parasitics begin to grow super-exponentially (until MRI termination at $t = 28.9$ ms) from a value of about 10 orders of magnitude smaller than the amplitude of the MRI.

4.2 Amplification factor

4.2.1 Dependence on the initial perturbations in Aenus

As we discuss in more detail in Appendix B, the boundary conditions used in simulations performed with AENUS do affect the exact value of the amplification factor and its dependence on the initial parasitic perturbations. Intuitively, one would expect (somewhat) larger amplification factor for smaller initial parasitic perturbations (see also Eqs. 47 and 54). However, independently of the initial perturbations, non-axisymmetric perturbations introduced by our radial boundary conditions can be used by parasitic instabilities as their seed perturbations. These can be seen when comparing the amplification factor of simulations #A8a, #A8b, #A8c, which are done with the same initial conditions (physical and numerical) but different realisations of random initial perturbations with the same normalisation δ . However, the amplification factor is basically the same in all three simulations, i.e. $\mathcal{A} \approx 21$.

This fact can be seen even more clearly when comparing simulations #A9a and #A9b. In the former, we used standard initial perturbations, whereas in the latter we put $k_z = 3k_{\text{MRI}}$ (see Eq. 59), i.e. we perturbed the system with a mode that should be stable against MRI (cf. PC08, Rembiasz et al. 2016a, for the instability criterion). The only difference between these two simulations was, that in the latter an MRI channel was formed a few milliseconds later and MRI was terminated ~ 10 ms later. However, the amplification factor was basically not affected ($\mathcal{A} = 21.0$ and $\mathcal{A} = 20.0$,

Table 2. Overview of our 3D MRI simulations done with SNOOPY. The columns are like in Tab. 1 but the initial perturbations are defined in equations (61)–(65).

#	b_{0z} [10^{13} G]	R_e	R_m	λ_{MRI} [km]	box size ($r \times \phi \times z$) [km]	resolution ($r \times \phi \times z$)	zones per channel	$\epsilon[10^{-5}]$	$\delta[10^{-5}]$	$\mathcal{M}_{\phi}^{\text{term}}$ [10^{28} G ²]	\mathcal{A}
S1a	0.12	100	100	0.067	$2 \times 2 \times 0.067$	$1920 \times 960 \times 64$	64	0.02	0.1	0.39	53.2
S1b	0.12	100	100	0.067	$2 \times 2 \times 0.067$	$1920 \times 960 \times 64$	64	0.02	0.1	0.34	49.3
S1c	0.12	100	100	0.067	$2 \times 2 \times 0.067$	$1920 \times 960 \times 64$	64	0.02	0.1	0.27	44.0
S1d	0.12	100	100	0.067	$2 \times 2 \times 0.067$	$1920 \times 960 \times 64$	64	0.02	0.1	0.32	48.2
S1e	0.12	100	100	0.067	$2 \times 2 \times 0.067$	$1920 \times 960 \times 64$	64	0.02	0.1	0.35	50.0
S2a	0.24	100	100	0.133	$2 \times 2 \times 0.133$	$960 \times 480 \times 64$	64	0.04	0.2	1.31	48.8
S2b	0.24	100	100	0.133	$2 \times 2 \times 0.133$	$960 \times 480 \times 64$	64	0.04	0.2	1.47	51.6
S2c	0.24	100	100	0.133	$2 \times 2 \times 0.133$	$960 \times 480 \times 64$	64	0.04	0.2	1.55	52.9
S2d	0.24	100	100	0.133	$2 \times 2 \times 0.133$	$960 \times 480 \times 64$	64	0.04	0.2	1.78	56.8
S2e	0.24	100	100	0.133	$2 \times 2 \times 0.133$	$960 \times 480 \times 64$	64	0.04	0.2	1.24	47.5
S3	0.59	100	100	0.333	$2 \times 2 \times 0.333$	$384 \times 192 \times 64$	64	0.1	0.5	11.77	58.4
S4	0.59	100	100	0.333	$2 \times 2 \times 0.333$	$768 \times 384 \times 128$	128	0.1	0.5	5.88	41.3
S5	0.64	100	100	0.364	$2 \times 2 \times 0.364$	$352 \times 176 \times 64$	64	0.11	0.55	11.37	52.6
S6	0.64	100	100	0.364	$2 \times 2 \times 0.364$	$704 \times 352 \times 128$	128	0.11	0.55	9.07	47.0
S7a	0.71	100	100	0.400	$2 \times 2 \times 0.400$	$320 \times 160 \times 64$	64	0.12	0.60	12.33	49.8
S7b	0.71	100	100	0.400	$2 \times 2 \times 0.400$	$320 \times 160 \times 64$	64	0.12	0.60	20.27	63.9
S7c	0.71	100	100	0.400	$2 \times 2 \times 0.400$	$320 \times 160 \times 64$	64	0.12	0.60	16.87	58.2
S7d	0.71	100	100	0.400	$2 \times 2 \times 0.400$	$320 \times 160 \times 64$	64	0.12	0.60	16.02	56.8
S7e	0.71	100	100	0.400	$2 \times 2 \times 0.400$	$320 \times 160 \times 64$	64	0.12	0.60	9.66	44.1
S8a	0.71	100	100	0.400	$2 \times 2 \times 0.400$	$640 \times 320 \times 128$	128	0.12	0.60	19.13	62.0
S8b	0.71	100	100	0.400	$2 \times 2 \times 0.400$	$640 \times 320 \times 128$	128	0.12	0.60	13.40	51.9
S8c	0.71	100	100	0.400	$2 \times 2 \times 0.400$	$640 \times 320 \times 128$	128	0.12	0.60	11.92	49.0
S8d	0.71	100	100	0.400	$2 \times 2 \times 0.400$	$640 \times 320 \times 128$	128	0.12	0.60	21.76	66.2
S8e	0.71	100	100	0.400	$2 \times 2 \times 0.400$	$640 \times 320 \times 128$	128	0.12	0.60	13.89	52.9
S9	0.78	100	100	0.444	$2 \times 2 \times 0.444$	$288 \times 144 \times 64$	64	0.13	0.67	20.4	57.7
S10	0.78	100	100	0.444	$2 \times 2 \times 0.444$	$576 \times 288 \times 128$	128	0.13	0.67	13.02	46.0
S11	0.88	100	100	0.500	$2 \times 2 \times 0.500$	$256 \times 128 \times 64$	64	0.15	0.75	20.75	51.7
S12	0.88	100	100	0.500	$2 \times 2 \times 0.500$	$512 \times 256 \times 128$	128	0.15	0.75	18.38	48.6
S13a	1.01	100	100	0.571	$2 \times 2 \times 0.571$	$224 \times 112 \times 64$	64	0.17	0.86	34.74	58.5
S13b	1.01	100	100	0.571	$2 \times 2 \times 0.571$	$224 \times 112 \times 64$	64	0.17	0.86	56.91	74.9
S13c	1.01	100	100	0.571	$2 \times 2 \times 0.571$	$224 \times 112 \times 64$	64	0.17	0.86	32.15	56.3
S13d	1.01	100	100	0.571	$2 \times 2 \times 0.571$	$224 \times 112 \times 64$	64	0.17	0.86	25.85	50.5
S13e	1.01	100	100	0.571	$2 \times 2 \times 0.571$	$224 \times 112 \times 64$	64	0.17	0.86	64.49	79.7
S14a	1.01	100	100	0.571	$2 \times 2 \times 0.571$	$448 \times 224 \times 128$	128	0.17	0.86	50.40	70.5
S14b	1.01	100	100	0.571	$2 \times 2 \times 0.571$	$448 \times 224 \times 128$	128	0.17	0.86	36.77	60.2
S14c	1.01	100	100	0.571	$2 \times 2 \times 0.571$	$448 \times 224 \times 128$	128	0.17	0.86	34.17	58.0
S14d	1.01	100	100	0.571	$2 \times 2 \times 0.571$	$448 \times 224 \times 128$	128	0.17	0.86	37.22	60.6
S14e	1.01	100	100	0.571	$2 \times 2 \times 0.571$	$448 \times 224 \times 128$	128	0.17	0.86	38.95	62.0
S15a	1.18	100	100	0.666	$2 \times 2 \times 0.666$	$192 \times 96 \times 64$	64	0.2	0.1	164.56	109.2
S15b	1.18	100	100	0.666	$2 \times 2 \times 0.666$	$192 \times 96 \times 64$	64	0.2	0.33	105.31	87.3
S15c	1.18	100	100	0.666	$2 \times 2 \times 0.666$	$192 \times 96 \times 64$	64	0.2	1	46.53	58.0
S15d	1.18	100	100	0.666	$2 \times 2 \times 0.666$	$192 \times 96 \times 64$	64	0.2	1	53.33	62.1
S15e	1.18	100	100	0.666	$2 \times 2 \times 0.666$	$192 \times 96 \times 64$	64	0.67	1	73.53	73.0
S15f	1.18	100	100	0.666	$2 \times 2 \times 0.666$	$192 \times 96 \times 64$	64	2	1	77.67	75.0
S15g	1.18	100	100	0.666	$2 \times 2 \times 0.666$	$192 \times 96 \times 64$	64	6.67	1	95.09	83.0
S15h	1.18	100	100	0.666	$2 \times 2 \times 0.666$	$192 \times 96 \times 64$	64	20	1	91.70	81.5
S16a	1.18	100	100	0.666	$2 \times 2 \times 0.666$	$384 \times 192 \times 128$	128	0.2	0.1	146.86	103.1
S16b	1.18	100	100	0.666	$2 \times 2 \times 0.666$	$384 \times 192 \times 128$	128	0.2	0.33	95.08	83.0
S16c	1.18	100	100	0.666	$2 \times 2 \times 0.666$	$384 \times 192 \times 128$	128	0.2	1	47.83	58.8
S16d	1.18	100	100	0.666	$2 \times 2 \times 0.666$	$384 \times 192 \times 128$	128	0.2	1	45.17	57.2
S16e	1.18	100	100	0.666	$2 \times 2 \times 0.666$	$384 \times 192 \times 128$	128	0.67	1	58.62	65.1
S16f	1.18	100	100	0.666	$2 \times 2 \times 0.666$	$384 \times 192 \times 128$	128	2	1	69.53	70.9
S16g	1.18	100	100	0.666	$2 \times 2 \times 0.666$	$384 \times 192 \times 128$	128	6.67	1	82.19	82.2
S16h	1.18	100	100	0.666	$2 \times 2 \times 0.666$	$384 \times 192 \times 128$	128	20	1	97.67	84.1
S17a	1.18	100	100	0.666	$2 \times 2 \times 0.666$	$768 \times 384 \times 256$	256	0.2	1	56.11	63.7
S17b	1.18	100	100	0.666	$2 \times 2 \times 0.666$	$768 \times 384 \times 256$	256	0.2	1	54.63	62.9
S18	1.18	100	100	0.666	$2 \times 2 \times 0.666$	$1536 \times 768 \times 512$	512	0.2	1	32.70	48.7
S19	1.18	100	100	0.666	$2 \times 2 \times 0.666$	$192 \times 96 \times 64$	64	0.2	1	101.58	84.2

Table 2 – *continued* Overview of our 3D MRI simulations done with SNOOPY, perturbations like in AENUS. The columns are like in Tab. 1 but the initial perturbations are defined in equations (61)–(65).

#	b_{0z} [10^{13} G]	R_e	R_m	λ_{MRI} [km]	box size ($r \times \phi \times z$) [km]	resolution ($r \times \phi \times z$)	zones per channel	ϵ [10^{-5}]	δ [10^{-5}]	$\mathcal{M}_{r\phi}^{\text{term}}$ [10^{28} G ²]	\mathcal{A}
SA15a	1.18	100	100	0.666	$2 \times 2 \times 0.666$	$192 \times 96 \times 64$	64	0.2	1	116.83	91.6
SA15b	1.18	100	100	0.666	$2 \times 2 \times 0.666$	$192 \times 96 \times 64$	64	0.2	1	106.44	87.4
SA15c	1.18	100	100	0.666	$2 \times 2 \times 0.666$	$192 \times 96 \times 64$	64	0.2	1	118.24	88.6
SA15d	1.18	100	100	0.666	$2 \times 2 \times 0.666$	$192 \times 96 \times 64$	64	0.2	1	118.24	92.2
SA15e	1.18	100	100	0.666	$2 \times 2 \times 0.666$	$192 \times 96 \times 64$	64	0.2	1	105.71	87.1
SCA15a	1.18	100	100	0.666	$2 \times 2 \times 0.666$	$192 \times 96 \times 64$	64	1233	22.7	35.52	50.5
SCA15b	1.18	100	100	0.666	$2 \times 2 \times 0.666$	$192 \times 96 \times 64$	64	1233	227	25.85	43.1
SCA15c	1.18	100	100	0.666	$2 \times 2 \times 0.666$	$192 \times 96 \times 64$	64	1233	227	24.68	42.1
SCA15d	1.18	100	100	0.666	$2 \times 2 \times 0.666$	$192 \times 96 \times 64$	64	1233	227	23.28	40.9
SCA15e	1.18	100	100	0.666	$2 \times 2 \times 0.666$	$192 \times 96 \times 64$	64	1233	2270	10.00	26.8
SCA15f	1.18	100	100	0.666	$2 \times 2 \times 0.666$	$192 \times 96 \times 64$	64	1233	2270	10.21	27.1
SCA15g	1.18	100	100	0.666	$2 \times 2 \times 0.666$	$192 \times 96 \times 64$	64	1233	2270	8.64	24.9
SCR15a	1.18	100	100	0.666	$2 \times 2 \times 0.666$	$192 \times 96 \times 64$	64	1233	227	5.78	20.4
SCR15b	1.18	100	100	0.666	$2 \times 2 \times 0.666$	$192 \times 96 \times 64$	64	1233	227	4.44	17.9
SCR15c	1.18	100	100	0.666	$2 \times 2 \times 0.666$	$192 \times 96 \times 64$	64	1233	227	7.25	22.8
SCA16a	1.18	100	100	0.666	$2 \times 2 \times 0.666$	$384 \times 192 \times 128$	128	1233	227	31.80	47.8
SCA16b	1.18	100	100	0.666	$2 \times 2 \times 0.666$	$384 \times 192 \times 128$	128	1233	227	30.17	46.6
SCA16c	1.18	100	100	0.666	$2 \times 2 \times 0.666$	$384 \times 192 \times 128$	128	1233	227	35.03	50.2

respectively). A more detailed discussion of this simulation can be found in Rembiasz (2013).

In spite of the boundary conditions used in AENUS simulations, we could say that because of the fact that due to these artificial non-axisymmetric perturbations, the amplification factor does not have any random scatter, this has the upside that we could perform convergence studies. On the other hand, in order to reliably assess the dependence of the amplification factor on the initial perturbations, we have validated the AENUS results by employing a completely different code, SNOOPY, where the boundary conditions are much easier to handle (though under the restrictions of applicability spelled out in Sect. 3.1.2).

4.2.2 Dependence on the initial perturbations in Snoopy

To test the dependence on the amplitude of the initial random perturbations, which are mainly a seed for KH parasitic instabilities, i.e. parameter δ in Eq. (59), we ran simulations #S15a–#S15d and #S16a–#S16d with the same initial magnetic field strength $b_{0z} = 1.18 \times 10^{13}$ G in all models, but with two different resolutions and varying amplitudes of the initial perturbations in the range $\delta = (0.1\text{--}1) \times 10^{-5}$ (upper panel of Fig. 3). We note that the models #S15c and #S15d have the same initialisation but, because of the stochastic nature of the initial perturbations they are run to assess the scatter of the final results as a function of the initial randomness imposed by the perturbations parametrised with the amplitude δ . The same comment applies to models #S16c and #S16d. The amplification factor is in the range $\mathcal{A} \approx 60\text{--}110$, which is by a factor $\sim 3\text{--}5$ larger than in AENUS simulations.

In order to test the influence of the initial channel amplitude on the amplification factor, we consider the sets of models #S15c–#S15h and #S16c–#S16h. Both sets differ in resolution and within each set we vary the initial channel amplitude in the range $\epsilon = (0.2\text{--}20) \times 10^{-5}$ (bottom panel of Fig. 3). We see a logarithmic dependence of the amplification factor on the amplitudes of both

the initial perturbations and of the channel modes. To these simulation results we fitted a function

$$\mathcal{A}(\epsilon, \delta) = a \ln \epsilon + d \ln \delta + C, \quad (74)$$

obtaining $a = 5.4 \pm 0.55$, $d = -20.2 \pm 1.2$, and $C = -101 \pm 13$. Now, we can compare these results with two different theoretical predictions for the amplification factor given by Eqs. (47) and (54). If we assume that $\tilde{v}_{\text{KH}} \propto \delta$, $\sigma = 0.27$, and $\ln \mathcal{A} \approx \text{const.}$ in this parameter range, from Eq. (47), we would theoretically expect $d = -1.85$. We obtain a discrepancy of one order of magnitude. When calculating the parasitic growth rate (Eq. 29), PG09 neglected the influence of the background shear (and of the Coriolis force) which, as pointed out by Latter et al. (2010) can lead to a reduction of the growth rate. Taking this effect into account in an approximate way, Eq. (54) predicts $d = -3.41$. Moreover, taking into account the growth of the magnetic field in the time interval τ by a factor of ≈ 3 (see the discussion below Eq. 54), would lead to $d = -10.1$, which is closer to the simulation results. This discrepancy could be caused by the extrapolation of Eq. (29) to the non-linear regime of the KH instability, where we, however, expect a growth rate reduction. Taking all these effects into account, we could expect a significant growth rate reduction. Note that from the fit we could estimate that the effective value of σ is $\sigma_{\text{eff}} = 0.0125$, i.e. the KH growth rate should be one order of magnitude lower than predicted by Eq. (29). However, we should recall that σ cannot really be a constant, since by definition, after saturation the parasitic modes should not grow any longer, implying $\sigma \rightarrow 0$. Very likely, the proportionality between γ and v_c expressed in Eq. (29) is a linearisation of a more general relation of the form $\gamma_{\text{KH}} = k_{\text{MRI}} f(v_c)$, where $f(v_c)$ is a non-linear function of the velocity of the MRI channels. However, exploring modifications of the parasitic model theory that include such kind of non-linearities is beyond the scope of this paper.

To study the dependence of the amplification factor on the initial channel amplitude, if we assume that $\tilde{v}_c \propto \epsilon$, $\sigma = 0.27$, and again $\ln \mathcal{A} \approx \text{const.}$ from Eqs. (47) and (54), we would theoret-

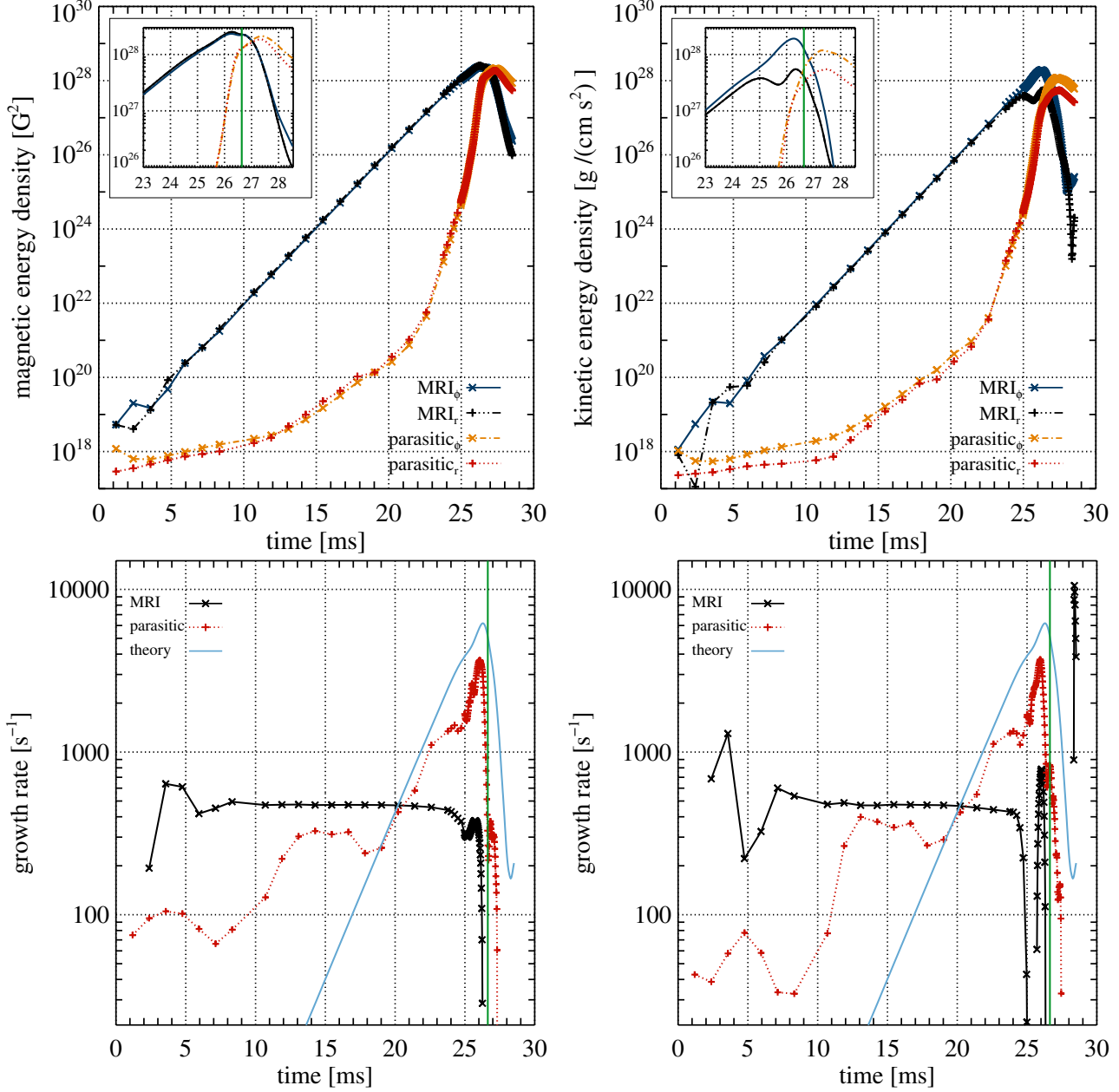


Figure 1. Time evolution of the MRI and parasitic modes in simulation #A8a. *Upper left:* average magnetic energy density associated with the MRI channels ($\epsilon_{\text{MRI},\alpha}$) and the parasitic instabilities ($\epsilon_{\text{p},\alpha}$) for different components b_α of the magnetic field. In the inset, the phase around the MRI termination is presented. The vertical green line denotes termination time, $t = 26.7$ ms. *Bottom left:* MRI and parasitic growth rate calculated from the b_r component. The theoretically expected growth rate of the parasitic instabilities (Eq. 29) is marked with the blue curve. *Upper right and bottom right* panels are analogous to their left counterparts, but for the velocity components.

ically expect $a = 0$, i.e. the amplification factor should be independent of ϵ (note that we neglected the last term in the RHS of Eq. (47), as $\frac{\bar{v}_c}{c_{A2}} \ll 1$ in our simulations). Thus, we conclude that present predictions within the parasitic instability model fail to predict this dependence correctly.

To test the dependence of the amplification factor not only on the amplitude of the initial perturbations but also their form, we ran simulations #SA15a-e obtaining $\mathcal{A} \approx 90$, which is somewhat higher than for the corresponding simulations #S15c-d for which $\mathcal{A} \approx 60$. Taking into account that the MRI termination is a highly

non-linear process, we conclude that there is some, but not very strong dependence.

Finally, it is worthwhile comparing predictions given by two different numerical codes for similar initial conditions. In the best resolved AENUS simulations with $b_{0z} = 1.22 \times 10^{13}$ G, i.e. models #A10 and #A11, we obtained $\mathcal{A} \approx 19$, which is a considerably smaller value than in analogous SNOOPY simulations, i.e. models #S15a-e (with $b_{0z} = 1.22 \times 10^{13}$ G) in which $\mathcal{A} \approx 90$. This difference can be probably attributed to the following fact. The imperfect radial boundary conditions continuously pollute the numerical data on the grid (see the bottom panel of Fig. B2). These perturbations

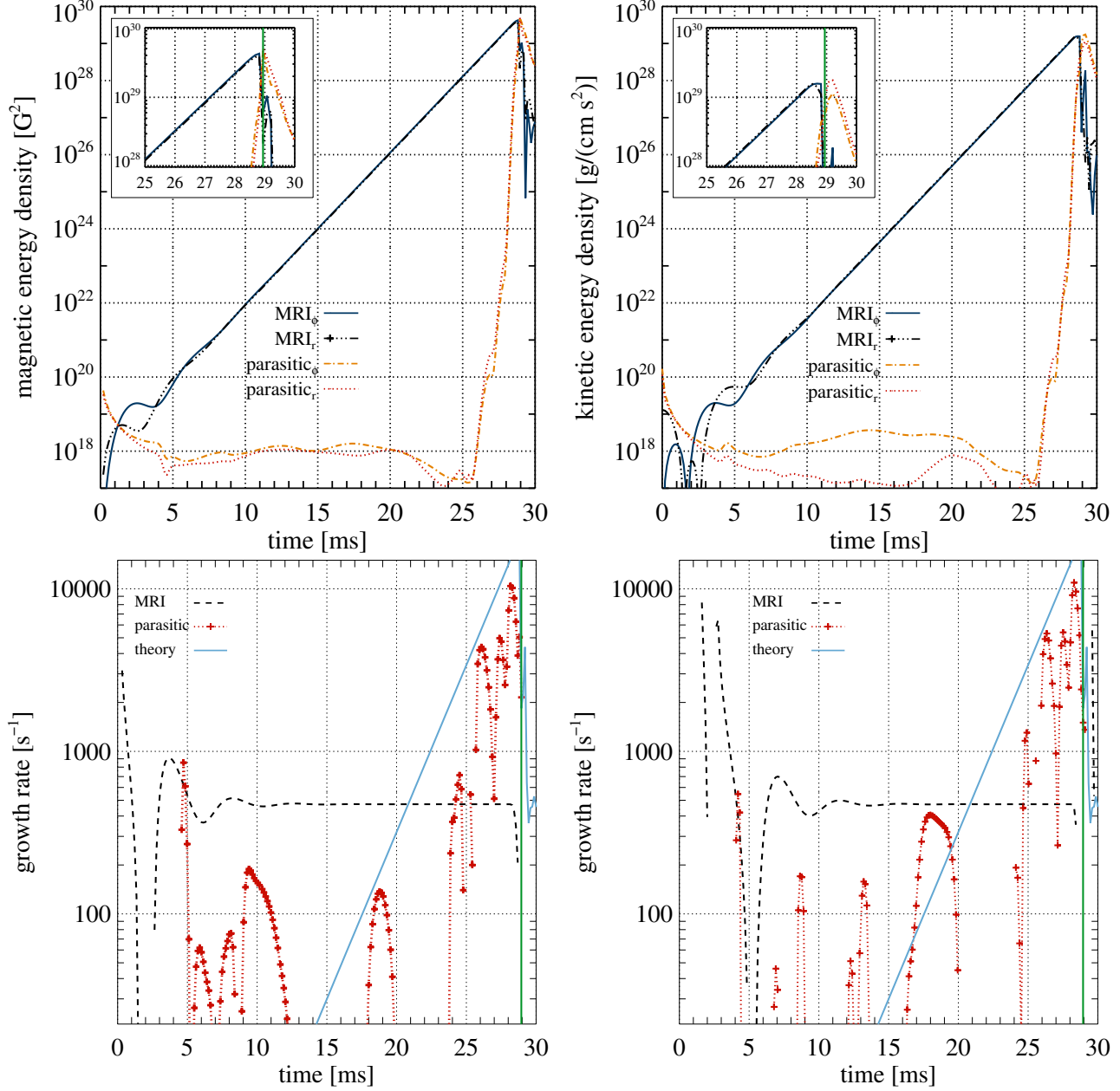


Figure 2. Same as Fig. 1, but for SNOOPY simulation #S19. The vertical green line denotes termination time $t = 28.8$ ms.

of both physical and numerical origin can act as seed perturbations for the parasitic instabilities. For AENUS, they seem to dominate the initial random perturbations of amplitude δ , which therefore are completely insignificant in comparison. Consequently, the termination of the MRI is decoupled from the parameter δ . Comparing the upper panels of Figures 1 and 2, we see that in the AENUS simulations, the non-axisymmetric perturbations grow from 5 to 20 ms, whereas they remain roughly constant in the SNOOPY simulations. In model #A8a, the non-axisymmetric perturbations start to grow super-exponentially with time from $t \approx 20$ ms. This can be attributed to the genuine parasitic instabilities. Therefore, we could equally well start this simulation at $t \approx 20$ ms with MRI channels determined by $\epsilon \approx 10^{-2}$ and random perturbations of roughly $\delta \approx 10^{-3}$. For these parameters, Eq. (74) yields an amplification factor $\mathcal{A}(\text{AENUS}) = 14 \pm 24$, i.e. smaller than 38, which is com-

patible with the value measured in the simulation, i.e. $\mathcal{A} = 18.6$ (for the amplitudes used in the actual simulation, i.e. $\delta = 10^{-5}$ and $\epsilon = 2 \times 10^{-6}$, the fitting formula predicts $\mathcal{A} = 61 \pm 34$, i.e. $\mathcal{A} > 27$). This result allows us to conclude that, if we account for the specific way the parasites are seeded, both sets of simulations can be understood by a common approximate theory, which we, thus, regard as a reasonable description of the physics.

To test this hypothesis, we ran additional SNOOPY simulations #SCA15a-g, #SCA15a-g, and #SCR15a-c with the same magnetic field strength, but much higher initial amplitudes (proportional to ϵ) of both full MRI channels (and not only perturbations in the v_r component which facilitated the development of the channels) and random perturbations (proportional to δ). In all these simulations we set $\epsilon = 1.2 \times 10^{-2}$ and $\delta = (0.02-2.27) \times 10^{-2}$, which should mimic the conditions in the AENUS simulation #A8a at $t \approx 21$ ms.

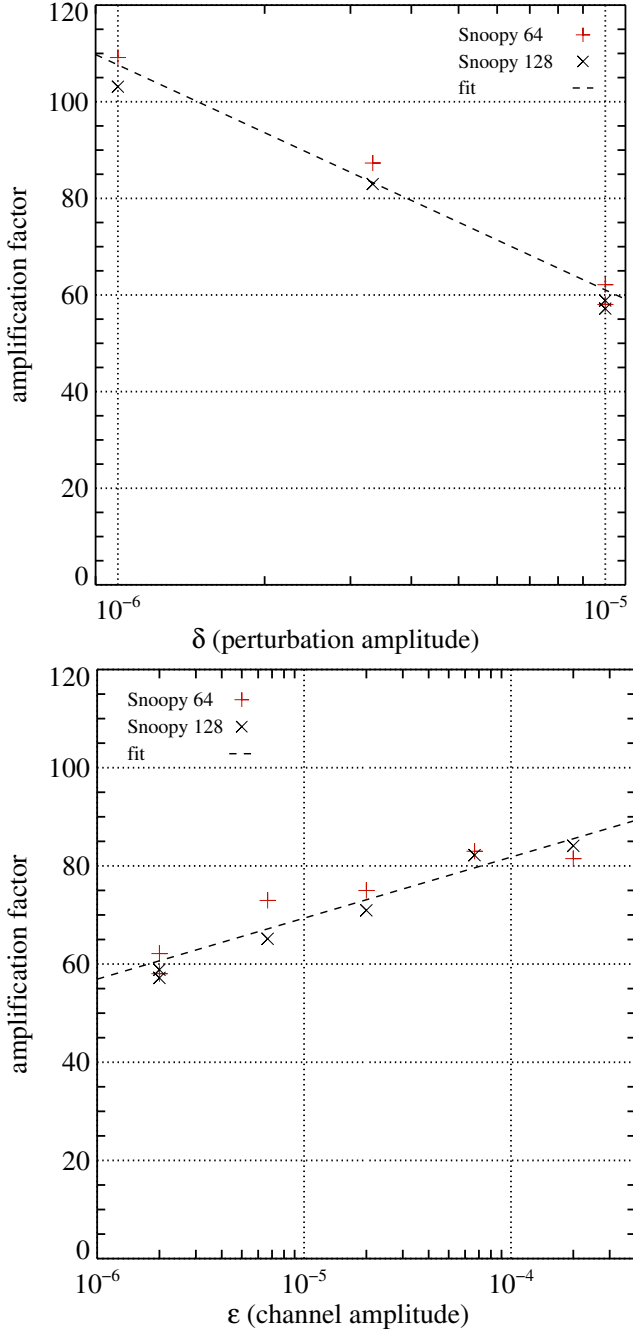


Figure 3. *Top:* amplification factor (defined in Eq. 35) dependence on the initial parasitic perturbations (proportional to δ , see Eq. 59) for simulations #S15a–#S15d (red plus symbols, 64 zones per MRI channel) and #S16a–#S16d (black crosses, 128 zones per MRI channel) done with SNOOPY. The fit to the data points was done according to Eq. (74). *Bottom:* amplification factor dependence on the initial channel perturbations (proportional to ϵ) for simulations #S15c–#S15h and #S16c–#S16h.

We measured in these additional SNOOPY simulations that the amplification factor indeed decreased by a factor of 2–3 to $\mathcal{A} \approx 18$ –50. This confirms our hypothesis that some part of the discrepancy between AENUS and SNOOPY simulations can be explained by spurious perturbations induced by the imperfect radial boundary conditions used in the former code.

We note that the differences (by a factor of 5) in the amplifica-

tion factor computed from AENUS and SNOOPY probably result from differences in the radial boundary conditions, the physical assumptions, and the numerical schemes employed in both codes.

4.2.3 Dependence on the initial magnetic field strength in Snoopy

Finally, we want to test the most relevant prediction of the parasitic model, i.e. the dependence of the amplification factor on the initial magnetic field strength. As in our simulations we used the most optimistic initial values for the magnetic field strength (i.e. $b_{0z} \approx 10^{13}$ G; Obergaulinger et al. 2014), it is of crucial importance to know whether in CCNSe with weaker initial magnetic fields the MRI will amplify the initial fields to the same value or by the same factor (or something in between). According to the estimate of PG09, the MRI should amplify the initial magnetic field by a constant factor (Eq. 37). However, their estimate was done using termination criterion I (Eq. 30), which as we have shown with our numerical models, is not an exact predictor of the MRI termination. According to our estimates done within the parasitic model using termination criterion II (Eq. 47), which as we have shown yields a much better prediction of the MRI termination, the amplification factor should be independent of the initial magnetic field strength provided that the ratio \tilde{v}_{KH}/c_{Az} is constant. Similarly, the estimate of \mathcal{A} that we can infer from Latter et al. (2010) (Eq. 54) also predicts no dependence on the initial magnetic field strength. Therefore, in order to address whether \mathcal{A} is independent from the initial magnetic field strength, we ran several numerical models.

In Fig. 4, we present all our best resolved models done with AENUS, i.e. #A4 #A6 and #A11 with the initial magnetic field strength $b_{0z} = (0.73\text{--}1.22) \times 10^{13}$ G, and all SNOOPY simulations with $b_{0z} = (0.12\text{--}1.18) \times 10^{13}$ G. Because of the scatter of the amplification factor in SNOOPY simulations, it was impossible to perform proper convergence tests (we would need many more simulations to compute proper averages). We ran only a few simulations with a very high resolution, i.e. 256 and 512 zones per MRI channel (models #S17a,b and #S18, respectively), which did not differ from those ran with lower resolutions. Therefore, we conclude that simulations done with 64 and 128 zones per MRI channels should give reasonably good predictions. We also marked in Fig. 4 the amplification factor estimated by PG09 (Eq. 37; light blue solid line) and us (dark blue dashed line) in Eq. (47) assuming initial parasitic amplitudes $\tilde{v}_{KH}/c_{Az} \approx 10^3$ (a representative value for our simulations). When looking at all our simulation results we can conclude that AENUS simulations give a value of \mathcal{A} lower by a factor of 1–6 than that obtained with SNOOPY. The discrepancy can be partly attributed to the boundary condition that we discussed before.

Beyond the code agreement on the exact value of \mathcal{A} , the amplification factor seems to be indeed independent of the initial magnetic field strength. This conclusion can be drawn on the light of the results of simulations #S1a–#S1e with an initial magnetic field lower by one order of magnitude than the rest of the models, i.e. $b_{0z} = 0.12 \times 10^{13}$ G. Even in these cases, the amplification factor stays the same within the random scatter, i.e. $\mathcal{A} \approx 50$ (Fig. 4).

Note that this result is also consistent with the results of Obergaulinger et al. (2009), who found a numerical scaling $\mathcal{M}_{r\phi}^{\text{term}} \propto b_{0z}^{16/7}$, which would translate to $\mathcal{A} \propto b_{0z}^{0.14}$ (i.e. a very weak dependence of the amplification factor on the initial magnetic field strength). Note, however, that as Obergaulinger et al. (2009) did not perform proper convergence studies, it is impossible to conclude based on their results whether this scaling law was of a physical or

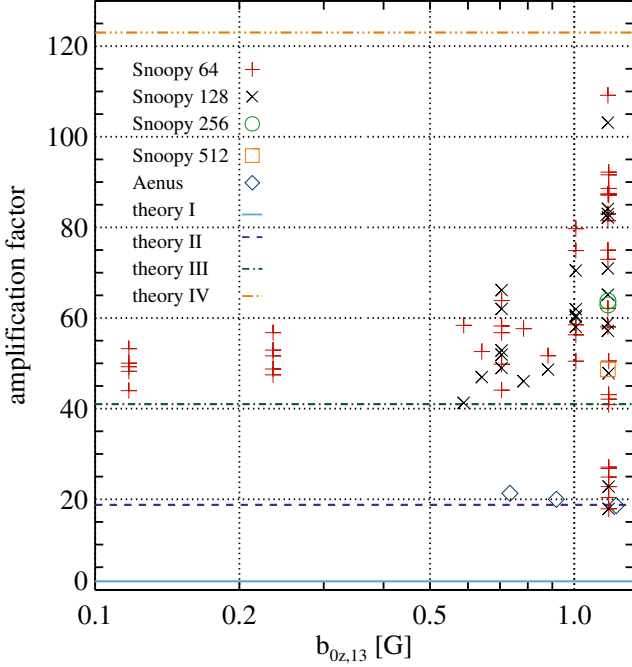


Figure 4. Amplification factor as a function of initial magnetic field in the best resolved simulations done with AENUS (i.e. models #A4 #A6 and #A11 from Tab. 1) and all simulations done with SNOOPY (Tab. 2). With light blue solid, purple dashed, green dash dot, and orange dash dot dot lines, we respectively marked theoretical estimates I (Eq. 37), II (Eq. 48), III (Eq. 55), and IV (Eq. 56) of the amplification factor. Note that the results shown for SNOOPY for the same initial magnetic field strength and resolution display a relatively large scattering as a result of the different initial amplitude of the perturbations.

of a numerical origin. Indeed, Rembiasz et al. (2016a) and Rembiasz et al. (2016b) observed dependence of $\mathcal{M}_{r\phi}^{\text{term}}$ on the numerical schemes and resolutions used in their studies.

5 SUMMARY

Since the direct numerical simulations of Obergaulinger et al. (2009) confirming the theoretical predictions of Akiyama et al. (2003), there is no doubt that the MRI can amplify the initial magnetic field (close to the surface of a PNS) on a sufficiently short time scale in CCSNe produced by rapidly rotating progenitors. However, the limit of such a magnetic field amplification during a CCSN explosion remained unknown. In this paper, we aimed to address an important aspect of this question, i.e. the factor by which the seed field of the core is amplified during the exponential growth phase of the MRI. To this end, we performed shearing disc simulations with an Eulerian MHD code, AENUS, solving full MHD equations and shearing box simulations with a pseudo-spectral code, SNOOPY, in the incompressible approximation. We compared our results to the predictions of the parasitic model proposed and developed by GX94, Latter et al. (2009), PG09 and Pessah (2010). Part of the predictions of the parasitic model, i.e. that given CCSN conditions, the MRI should be terminated by parasitic KH instabilities was confirmed in direct numerical simulations of Rembiasz et al. (2016a). However, those authors neither performed systematical studies of the amplification factor dependence on the initial conditions, nor

compared the field amplification obtained in their simulations to the predictions of the parasitic model.

Within the parasitic-termination model, the MRI channel modes are susceptible to secondary instabilities, in our case of KH type. The former grow at a constant rate given by the rotational profile of the core, whereas the growth rate of the former is a function of the amplitude of the MRI and, thus, increases continuously. At some point, they will be sufficiently strong to disrupt the MRI channel modes and thereby terminate the MRI growth. Based on this observation, PG09 proposed two different criteria to identify the moment of parasitic termination in their analytic model: termination occurs when the growth rate of (initially developing much more slowly) parasitic instabilities starts to exceed the growth rate of MRI (termination criterion I), or when the amplitudes of the parasitic instabilities reach the amplitudes of the MRI channels (termination criterion II).

We tested these two termination criteria and found that in simulations done with both codes, termination criterion II represents a better description of the results. MRI termination occurs when parasitic instabilities roughly reach the amplitudes of the MRI channels, which happens roughly $3\gamma_{\text{MRI}}^{-1}$ after termination criterion I is met.

Next, we compared the theoretical predictions of Pessah (2010), Latter et al. (2010) and our estimates based on Pessah (2010) for the amplification factor with our simulation results. We find an order-of-magnitude agreement of Latter's model with the numerical simulations, although this model fails to explain all dependencies accurately. This better agreement could be due to the approximate inclusion of the background shear by Latter et al. (2010). However, differences could also be due to non-linearities at termination, not considered in any theoretical estimate. From our numerical results we cannot favour any of those possibilities. Nevertheless, a more elaborate description of the parasitic instabilities in the presence of shear may be needed for an accurate prediction of the termination amplitude.

Another prediction of these simplified models is that the amplification factor should be independent of the initial magnetic field strength. We tested this hypothesis with numerical simulations. Our main finding of this paper is that independently of the initial magnetic field strength, the MRI channel modes can amplify the seed magnetic field by a factor of 20 to 100. Once these magnetic field values are reached, further MRI-driven magnetic field amplification is halted as the MRI channels are attacked and destroyed by parasitic KH instabilities.

It is true that, in principle, one could obtain an arbitrary value of the amplification factor from our scaling relation (Eq. 74) by tuning the amplitudes of the initial perturbations. However, for physically plausible conditions found at the surface of the hot proto-neutron star, the initial amplitudes are more likely to be of the order ~ 0.1 – 1 of the rotational velocity. Under these conditions, realistically expected values of the amplification factor are of the order of 10. In any case, even for a highly unperturbed flow with perturbations $\sim 10^{-5}$ we could not find amplification factors exceeding ~ 100 . We stress that our results have been obtained under the most favourable conditions for the MRI to develop concerning location and geometry of our computational boxes. The fact that the boxes are located in the equatorial plane of the PNS optimises the topology of the magnetic field for the fastest possible growth (see, e.g. Balbus & Hawley 1998). If even under these *optimal* conditions the ability of the MRI channels as an agent to amplify the initial field is limited, we shall expect that anywhere else in the PNS the MRI channel-mode amplification be even smaller.

While our simulations allow us to draw conclusions on the field amplification by MRI channel modes, their applicability beyond the linear, local MRI modes needs to be assessed critically:

- The MRI might take other forms than that of channels (e.g. global modes) under realistic conditions especially for slower rotation rates.
- Even if non-local modes can be excluded, the channels might not appear at all due to the presence of other instabilities. As we have shown here, strong perturbations may quench the MRI channel modes very early, hence reinforcing our conclusion that the amplification is limited.
- The long-lasting turbulent phase after the disruption of channels might strongly modify the amplification achieved by the channel modes because an MRI-driven dynamo could be at work during this phase.

The main conclusion that should be drawn by the supernova community is that the amount of field amplification the MRI channels might provide in CCSNe might be fairly limited. This finding casts doubt on the common procedure of starting global simulations with artificially enhanced field strengths that is based on the expectation that the MRI will provide rapid amplification of even very weak initial fields up to equipartition levels with the kinetic (rotational) energy. This may be true if an MRI-driven turbulent dynamo develops sufficiently fast and efficiently.

Beyond the implications for CCSNe, we also point out that our results are relevant for the standard setup assumed in models of progenitors of gamma-ray bursts. In those models a fairly large magnetic field ($\gtrsim 10^{15}$ G) is needed to extract an ultrarelativistic outflow fed by the rotational energy of the central compact object. Regardless of whether such an object is a proto-magnetar or a black hole, our findings suggest that the progenitor star should be endowed with an uncommonly large magnetic field prior to core collapse. Alternatively, a large-scale turbulent dynamo, driven either by rapid rotation and convection, or by the MRI, might be able to operate on longer timescales (Thompson & Duncan 1993). However, it still remains to be proven that this is the case in global simulations, starting from realistic progenitors. This has been explored recently by Mösta et al. (2015), albeit in a regime in which magnetic field is already of magnetar strength.

Additionally, one should bear in mind the limitations of our studies in which we neglected the influence of neutrinos (see Guilet et al. 2015), buoyancy and entropy gradients (see Obergaulinger et al. 2009; Guilet & Müller 2015). Nevertheless, we do not think that including these effects could lead to much stronger magnetic field amplification by the MRI channel modes. Moreover, we did so far not consider any possible additional field amplification by a MRI-driven dynamo acting in the turbulent saturated state after the end of MRI channel mode growth. However its influence on the MRI termination as well as the influence of compressibility remain unknown.

APPENDIX A: RESCALING OF THE SIMULATIONS OF REMBIASZ ET AL. (2016A)

Rembiasz et al. (2016a), following Obergaulinger et al. (2009), performed almost ideal MHD (i.e. with $R_e, R_m \gtrsim 100$) simulations in a computational domain centred around the equatorial plane at a radius $\tilde{r}_0 = 15.5$ km, i.e. in middle of a nascent PNS of radius $r_{\text{PNS}} \approx 30$ km. However, according to the recent estimates of Guilet

et al. (2015), at these distances the neutrino viscosity cannot be neglected and it can suppress the MRI. Therefore, since the models can be suitably rescaled, we shifted the centre of their computational domain close to the surface of the PNS, i.e. $r_0 = 31$ km, as it is the most favourable place for the development of the MRI. At this location, the differential rotation gradient and the Reynolds numbers are larger than deep inside the PNS.

In the current publication, we discussed some of the simulations already presented in Rembiasz et al. (2016a), but this time with the initial conditions rescaled to the properties likely present at the surface of the PNS. The key physical quantities have been rescaled in the following way:

$$\mathcal{M}_{r\phi} = \tilde{\mathcal{M}}_{r\phi} \left(\frac{r_0}{\tilde{r}_0} \right)^2 \left(\frac{\Omega_0}{\tilde{\Omega}_0} \right)^2 \left(\frac{\rho_0}{\tilde{\rho}_0} \right) \quad (\text{A1})$$

$$b = \tilde{b} \left(\frac{r_0}{\tilde{r}_0} \right) \left(\frac{\Omega_0}{\tilde{\Omega}_0} \right) \left(\frac{\rho_0}{\tilde{\rho}_0} \right)^{1/2} \quad (\text{A2})$$

$$t = \tilde{t} \left(\frac{\Omega_0}{\tilde{\Omega}_0} \right)^{-1} \quad (\text{A3})$$

$$\lambda_{\text{MRI}} = \tilde{\lambda}_{\text{MRI}} \left(\frac{r_0}{\tilde{r}_0} \right) \quad (\text{A4})$$

$$\gamma_{\text{MRI}} = \tilde{\gamma}_{\text{MRI}} \left(\frac{\Omega_0}{\tilde{\Omega}_0} \right), \quad (\text{A5})$$

$$L_i = \tilde{L}_i \left(\frac{r}{r_0} \right), \quad (\text{A6})$$

where quantities with tilde are the values used by Rembiasz et al. (2016a), i.e. $\tilde{\Omega}_0 = 1824 \text{ s}^{-1}$ and $\tilde{\rho}_0 = 2.47 \times 10^{13} \text{ g cm}^{-3}$, and in the current paper, we set $\Omega_0 = 767 \text{ s}^{-1}$, and $\rho_0 = 2.47 \times 10^{12} \text{ g cm}^{-3}$. In Tab. A1, we present the list of the simulations that were presented in both papers.

APPENDIX B: TECHNICAL DETAILS

In this appendix, we assess the quality of the numerical results obtained with AENUS. To this end, we analyse in more detail simulation #A8a performed with AENUS (presented Sec. 4.1.1) as well as, we compare it with simulation #S19 performed with SNOOPY (Sec. 4.2.2).

In both simulations the MRI channel modes experience a very similar evolution with the differences being visible only shortly before their termination (see Figs. 1 and 2). The time evolution of the parasitic modes differs almost from the beginning of the simulations, however. To investigate this difference in more detail, we note that the dominant axisymmetric MRI modes (with a vanishing radial component of the wavevector) do not amplify the v_z component of the velocity. Hence, we could tentatively use this component as a tracer of the parasitic instabilities if no other (numerical) effects drive the growth of v_z . If we define

$$e_z^{\text{kin}} \equiv \frac{\int \frac{1}{2} \rho v_z^2 dV}{\int dV}, \quad (\text{B1})$$

then

$$\gamma_z \equiv \frac{\dot{e}_z^{\text{kin}}}{2e_z^{\text{kin}}}, \quad (\text{B2})$$

should in principle be equal to the growth rate of the parasitic instabilities (provided there are no other effects affecting v_z). In the upper panel of Fig. B1 we provide a comparison between the time evolution of γ_z and that of the MRI growth rate computed from

Table A1. List of the simulations done with AENUS presented in Rembiasz et al. (2016a) and in the current paper. The simulation identifier ,#, used by Rembiasz et al. (2016a) and in the current paper, is shown in the left and in the right column, respectively.

Rembiasz et al. (2016a)	current paper
5	A7
7	A8a
9	A9a
10	A10
11	A11

the box-integrated v_z component of the velocity field in simulation #A8a.³ It is evident that γ_z follows quite closely the evolution of γ_{MRI} , specially in the time interval between $t \approx 12$ ms and $t \approx 21$ ms, instead of tracing the evolution of the growth rate of the parasitic instabilities (compare Fig. B1 upper panel with the lower right panel of Fig. 1). Hence, the growth of e_z^{kin} until $t \approx 21$ ms, cannot be caused (only) by parasitic instabilities. Indeed, Rembiasz (2013) observed a very similar behaviour of e_z^{kin} in his 2D and 3D MRI simulations performed with AENUS (see Figs. 4.13 and 4.14 therein), which hints that e_z^{kin} is amplified by an axisymmetric phenomenon (different from the dominant MRI axisymmetric modes).

This growth of e_z^{kin} can be explained by the following reasons. Firstly, as MRI magnetic channels grow, they will generate a non-uniform magnetic pressure accelerating fluid in the vertical direction (towards magnetic null surfaces of the MRI channels, cf. GX94). Secondly, the initially purely radial profile of the gas pressure will acquire a vertical gradient due to the advective transport of internal energy in the up- and down-flows of the channel modes. This in turn will create pressure gradients in the vertical direction and hence vertical fluid motions to redistribute the pressure and equilibrate the system. Thirdly, this vertical motions could be related to the radial boundary conditions. The MRI growth rate is not constant in the whole computational domain, as $\gamma_{\text{MRI}} \propto \Omega(r)$. This means that the amplitude of the channel modes will grow at a higher rate at $r = 30$ km than at $r = 32$ km. Consequently, once the MRI channels are formed, there is a shear at the radial boundaries where we use periodic boundary conditions for the perturbations. This shear introduces some perturbations to all velocity and magnetic field components, whose influence can be best observed in the v_z velocity component as it should not be affected by the dominant MRI mode. During the exponential growth phase, the amplitude of v_z is proportional to the amplitude of the MRI channels, v_c , so that, $|v_z| \approx 0.15v_c$.

A comparison of the upper panel of Fig. B1 with an analogous plot for simulation #S19 done with SNOOPY (bottom panel of Fig. B1) provides another argument supporting our hypothesis that those axisymmetric vertical motions are mostly of the numerical origin. In the SNOOPY simulation, the growth of the vertical motions, quantitatively indicated by γ_z , from $t \approx 12$ ms–17 ms is triggered by a subdominant axisymmetric MRI mode with a non-zero radial component. Note that γ_z becomes comparable to γ_{MRI} only when the genuine parasitic instabilities start to grow superexponentially.

However, as much as part of those vertical motions in the AENUS simulation is clearly of a numerical origin, we should not be concerned too much with that. Even though these axisymmetric

modes are dominant ‘non-MRI’ modes before real parasitic instabilities appear, they do not cause the MRI termination. In spite of the fact that the amplitude of these artificial modes is some 15% of the channel modes, the MRI can grow unaffected by them.

This can be clearly again seen with the help of Fourier analysis (see the upper panel of Fig. B2). Until $t = 23.8$ ms, the axisymmetric modes of v_z account for 99% of the kinetic energy stored in the v_z component. However, once the parasitic instabilities appear and start to contribute to this component, the fraction of the axisymmetric modes v_z drops significantly and very rapidly. At $t = 25.6$ ms, the contribution of axisymmetric modes to e_z^{kin} is 86%, and only half a millisecond later, i.e. at $t = 26.2$ ms, 16%. At the MRI termination, i.e. $t = 26.7$ ms, the total contribution of the axisymmetric modes is only 2.5%. This clearly demonstrates that those modes do not play a decisive role in the MRI termination and that the instability is terminated by genuine non-axisymmetric parasitic modes.

Another difference between the AENUS and SNOOPY simulations is that in the former, non-axisymmetric \hat{b}_a and \hat{w}_a modes grow from the beginning of the simulation, though until $t \approx 21$ ms at a rate lower than γ_{MRI} (upper panels of Fig. 1), whereas in the latter, these modes basically do not grow until $t \approx 25$ ms (upper panels of Fig. 2). This suggests that in the AENUS simulation, radial boundary conditions introduce also some non-axisymmetric perturbations (which in turn could be used as seed perturbations for genuine non-axisymmetric parasitic modes). To test this hypothesis, we compute the vertically and azimuthally averaged RMS amplitude of the non-axisymmetric part of the velocity component v_z , i.e.

$$\langle v_z(r) \rangle \equiv \sqrt{\frac{\int \int [v_z(r, \phi, z) - \bar{v}_z(r, z)]^2 d\phi dz}{\int d\phi \int dz}}, \quad (\text{B3})$$

where

$$\bar{v}_z(r, z) \equiv \frac{\int v_z(r, \phi, z) d\phi}{\int d\phi}, \quad (\text{B4})$$

before the termination (bottom panel of Fig. B2). From this panel, we can see that the non-axisymmetric part of the velocity component v_z is highest close to the radial boundaries. This suggests that radial boundary conditions are (most likely) responsible for triggering this component. However, only when the growth rate of the genuine parasitic modes is high enough, the parasitic modes can use those artificial modes as their initial perturbations. At later stages (and at the termination), the non-axisymmetric modes are not localised at the radial boundaries.

ACKNOWLEDGMENTS

TR acknowledges support from The International Max Planck Research School on Astrophysics at the Ludwig Maximilians

³ Note the difference with the value of the MRI growth rate shown in Fig. 1, which is computed from the Fourier transformed v_z component.

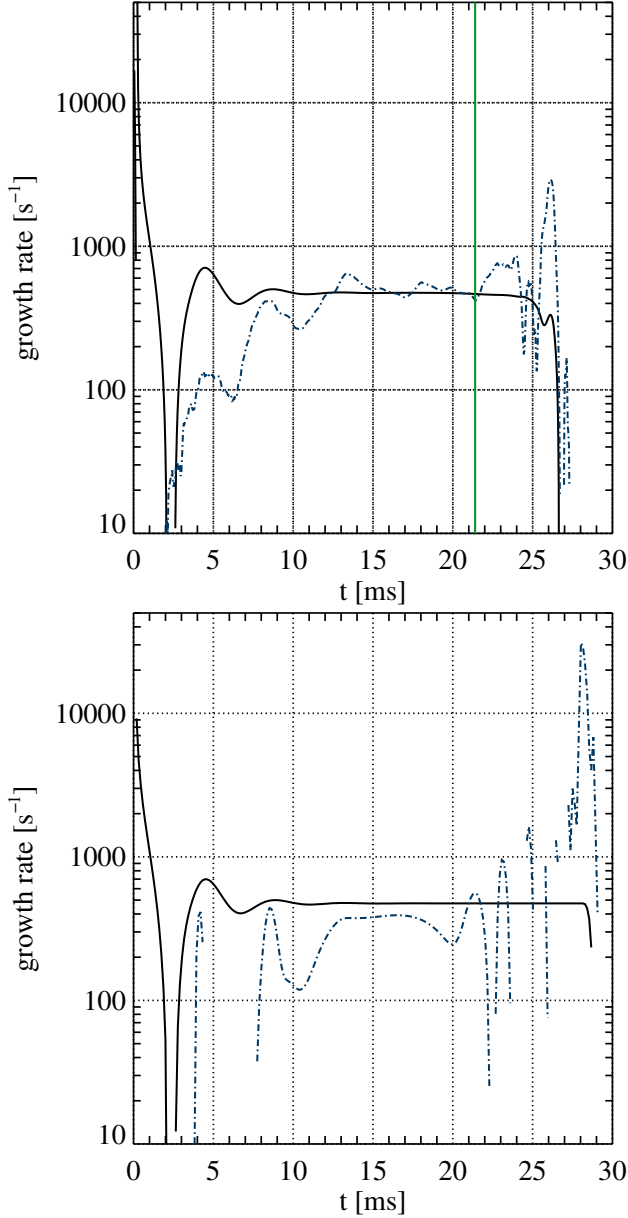


Figure B1. *Top:* Growth rate of the MRI (black line) and growth rate of the kinetic energy density in the vertical direction (dash-dotted line; Eq. B2) in AENUS simulation #A8a. Note that to properly compare both growth rates, the MRI growth rate is computed from the time evolution of the volume-averaged Maxwell stress (Eq. 34), instead of from the corresponding Fourier modes (as done in Fig. 1). The vertical green line marks the time at which the bottom snapshot of Fig. B2 is taken. *Bottom:* Same as the upper panel but for the Snoopy simulation #S19.

University Munich, JG, EM & TR acknowledge support from the Max-Planck-Princeton Center for Plasma Physics, and MA, PCD, TR and MO acknowledge support from the European Research Council (grant CAMAP-259276). We also acknowledge support from grants AYA2013-40979-P, AYA2015-66899-C2-1-P and PROMETEOII/2014-069. The authors thank M. Pessah, C. McNally and H. Latter for helpful discussions. The computations have been performed at the Leibniz Supercomputing Center of the Bavarian Academy of Sciences and Humanities (LRZ), the

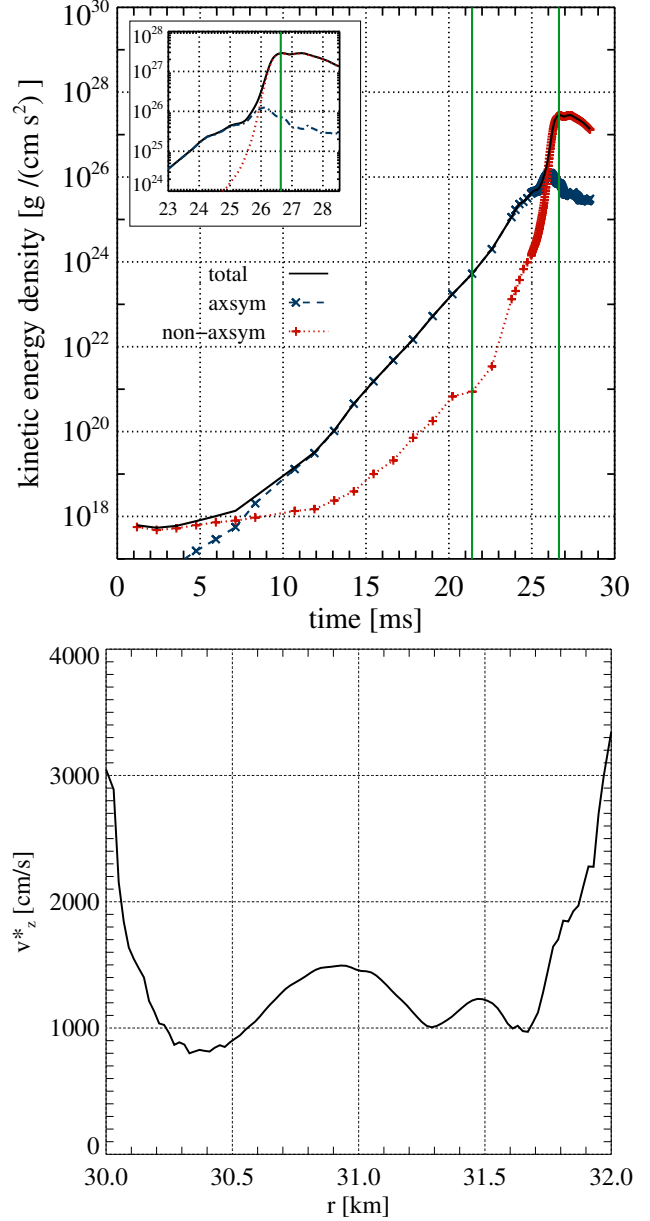


Figure B2. *Top:* Evolution of the kinetic energy density, and its axisymmetric and non-axisymmetric components for the AENUS model #A8a. *Bottom:* Vertically and azimuthally averaged RMS amplitude of the non-axisymmetric part of the velocity component, $\langle v_z(r) \rangle$ (Eq. B3) for the same AENUS model as in the upper panel.

Rechenzentrum Garching of the Max-Planck-Gesellschaft (RZG), and at the Servei d'Informàtica of the University of Valencia.

REFERENCES

- Akiyama, S., Wheeler, J. C., Meier, D. L., & Lichtenstadt, I. 2003, *ApJ*, 584, 954
- Balbus, S. A. 1995, *ApJ*, 453, 380
- Balbus, S. A. & Hawley, J. F. 1991, *ApJ*, 376, 214
- Balbus, S. A. & Hawley, J. F. 1998, *Reviews of Modern Physics*, 70, 1
- Brandenburg, A. 2005, *Astronomische Nachrichten*, 326, 787

- Cerdá-Durán, P., Font, J. A., Antón, L., Müller, E. 2008, *A&A*, 492, 937
- Chandrasekhar, S. 1960, *Proceedings of the National Academy of Science*, 46, 253
- Endeve, E., Cardall, C., Budiardja, R., & Mezzacappa, A. 2010, *ApJ*, 713, 1219
- Evans, C. R. & Hawley, J. F. 1988, *ApJ*, 332, 659
- Fromang, S. & Papaloizou, J. 2007, *A&A*, 476, 1113
- Gardiner, T. A. & Stone, J. M. 2005, in *American Institute of Physics Conference Series*, Vol. 784, *Magnetic Fields in the Universe: From Laboratory and Stars to Primordial Structures.*, ed. E. M. de Gouveia dal Pino, G. Lugones, & A. Lazarian, 475–488
- Goldreich, P. & Lynden-Bell, D. 1965, *MNRAS*, 130, 125
- Goodman, J. & Xu, G. 1994, *ApJ*, 432, 213
- Guilet, J., Müller, E. & Janka, H. T. 2015, *ApJ*, 447, 3992
- Guilet, J. & Müller, E. 2015, *MNRAS*, 450, 2153
- Harten, A. 1983, *J. Comput. Phys.*, 49, 357
- Keppens, R., Tóth, G., Westermann, R. H. J., & Goedbloed, J. P. 1999, *Journal of Plasma Physics*, 61, 1
- Klahr, H. H. & Bodenheimer, P. 2003, *ApJ*, 582, 869
- Knobloch, E. & Julien, K. 2005, *PhFl*, 17, 094106
- Latter, H. N., Lesaffre, P., & Balbus, S. A. 2009, *MNRAS*, 394, 715
- Latter, H. N., Fromang, S., & Gressel, O. 2010, *MNRAS*, 406, 848
- Latter, H. N. 2016, *MNRAS*, 455, 2608
- Lesur G., Longaretti P.-Y., 2005, *A&A*, 444, 25
- Lesur G., Longaretti P.-Y., 2007, *MNRAS*, 378, 1471
- Lesur G., Longaretti P.-Y., 2011, *A&A*, 528, A17
- Longaretti P.-Y., Lesur G., 2010, *A&A*, 516, A51
- LeVeque, R. J. 1992, *Numerical Methods for Conservation Laws*, 2nd edn.
- Levy, D., Puppo, G., & Russo, G. 2002, *SIAM J. Sci. Comput.*, 24, 480
- Masada, Y., Takiwaki, T., & Kotake, K. 2015, *ApJL*, 798, L22
- Meheut, H., Fromang, S., Lesur, G., Joos, M., & Longaretti, P.-Y. 2015, *A&A*, 579, A117
- Meier, D. L., Epstein, R. I., Arnett, W. D., & Schramm, D. N. 1976, *ApJ*, 204, 869
- Menou, K., Balbus, S. A., & Spruit, H. C. 2004, *ApJ*, 607, 564
- Miyoshi, T., & Kusano, K. 2005, *Journal of Computational Physics*, 208, 315
- Mösta, P. and Ott, C. D. and Radice, et al. 2015, *Nature*, 528, 376
- Obergaulinger, M., Aloy, M. A., & Müller, E. 2006a, *A&A*, 450, 1107
- Obergaulinger, M., Aloy, M. A., Dimmelmeier, H., & Müller, E. 2006b, *A&A*, 457, 209
- Obergaulinger, M. 2008, PhD thesis, Technische Universität München
- Obergaulinger, M., Cerdá-Durán, P., Müller, E., & Aloy, M. A. 2009, *A&A*, 498, 241
- Obergaulinger, M., Aloy, M. A., Müller, E. 2010, *A&A*, 515, A30
- Obergaulinger, M., Janka, H.-T., & Aloy, M. A. 2014, *MNRAS*, 445, 3169
- Pessah, M. E., & Chan, C.-k. 2008, *ApJ*, 684, 498
- Pessah, M. E., & Goodman, J. 2009, *ApJL*, 698, L72
- Pessah, M. E. 2010, *ApJ*, 716, 1012
- Rembiasz, T. 2013, PhD thesis, Technische Universität München. <https://mediatum.ub.tum.de/doc/1183388>
- Rembiasz, T., Obergaulinger, M., Cerdá-Durán, P., Müller, E., & Aloy, M. A. 2016, *MNRAS*, 456, 3782
- Rembiasz, T., Obergaulinger, M., Cerdá-Durán, Aloy, M.-Á., & P., Müller, E. 2016, *Journal of Physics: Conference Series*, 719, 1, 012009
- Rempel E. L., Lesur G., Proctor M. R. E., 2010, *Physical Review Letters*, 105, 044501
- Sano, T. & Inutsuka, S.-i. 2001, *ApJL*, 561, L179
- Sano, T., Inutsuka, S.-i., Turner, N. J., & Stone, J. M. 2004, *ApJ*, 605, 321
- Sawai, H., Yamada, S., & Suzuki, H. 2013, *ApJ*, 770, L19
- Sawai, H., & Yamada, S., 2016, *ApJ*, 817, 153
- Shakura, N. I. & Sunyaev, R. A. 1973, *A&A*, 24, 337
- Suresh, A. & Huynh, H. 1997, *J. Comput. Phys.*, 136, 83
- Thompson, C. & Duncan, R. C. 1993, *ApJ*, 408, 194
- Toro, E. F. & Titarev, V. A. 2006, *J. Comput. Phys.*, 216, 403
- Velikhov, E. 1959, *Sov. Phys. JETP*, 36, 995
- Walker, J., Lesur, G., & Boldyrev, S. 2015, *MNRAS*, 457, L39
- Winteler, C., Käppeli, R., Perego, A., Arcones A., Vasset N., Nishimura N., Liebendörfer M., Thielemann F.-K., 2012, *ApJ*, 750, L22